

Synthesis of $\text{Ti}_3\text{C}_2\text{T}_{x(\text{exf})}\text{@h-BN@Co}_3\text{O}_4$ Hierarchical Structure: An Active Cathode for High-Performing Solid-State Supercapacitor and Density Functional Theory Calculations

Sarifa Regina Fernandes, Rajeshvari Samatbhai Karmur, Krishna Aravind Padmalayam, Ashakiran Maibam, Derek Hao, Ravichandar Babarao, and Narendra Nath Ghosh*

Herein, the synthesis of $\text{Ti}_3\text{C}_2\text{T}_{x(\text{exf})}\text{@h-BN@Co}_3\text{O}_4$ and its electrochemical performances as an active cathode material in a flexible all-solid-state asymmetric supercapacitor (ASC) is presented. A hierarchical heterostructure has been created by integrating nanometer-thin exfoliated $\text{Ti}_3\text{C}_2\text{T}_{x(\text{exf})}$ MXene sheets with a 2-D layered hexagonal boron nitride (h-BN) and immobilizing Co_3O_4 nanorods on the surface. h-BN and Co_3O_4 offer rich redox features and highly conductive $\text{Ti}_3\text{C}_2\text{T}_x$ facilitates the charge transfer process. To prepare the anode of ASC, a spent tea-derived porous carbon (PC) was used. An ASC device ($\text{Ti}_3\text{C}_2\text{T}_{x(\text{exf})}\text{@h-BN@Co}_3\text{O}_4/\text{PC}$) was assembled with PVA-KOH gel-electrolyte. This device exhibited a specific capacitance

of 105.8 F g^{-1} at a current density of 0.5 A g^{-1} , an energy density of 33.0 Wh kg^{-1} at a power density of 375 W kg^{-1} , and retention of $\approx 90\%$ of its initial capacitance and $\approx 85\%$ of its Coulombic efficiency after 5000 charge-discharge cycles. To gain an in-depth understanding of the electronic band structure of $\text{Ti}_3\text{C}_2\text{@h-BN@Co}_3\text{O}_4$, computational investigations were carried out. The calculated value of quantum capacitance of $\text{Ti}_3\text{C}_2\text{@h-BN@Co}_3\text{O}_4$ was $59.16 \mu\text{F cm}^{-2}$ at 2.67 V (positive bias). This work highlights the exceptional performance and durability of $\text{Ti}_3\text{C}_2\text{T}_{x(\text{exf})}\text{@h-BN@Co}_3\text{O}_4$ ternary heterostructure and positions it as a highly promising candidate for next-generation supercapacitors.

1. Introduction

Energy conversion and storage are both crucial for addressing the global challenges, including energy demand, environmental pollution, etc.^[1] and it has been recognized as an essential component for sustainable development within the 17 United Nations Sustainable Development Goals (SDGs) to set a sustainable agenda for 2030 and beyond.^[2] The foremost pursuit of SDG 7 has been to provide access to affordable and clean energy due to the increasing demand for energy supply and more stringent standards for environmental quality.^[3] To meet the growing energy requirement for our day-to-day life and simultaneously to address the increase of global pollution as a result of the exorbitant use of

fossil fuels, there is an urgent need to focus on green energy generation and the development of suitable technologies.^[4] However, the intermittent availability of renewable energy sources (such as wind, hydro, tidal, solar, etc) and their unreliable quality surges the need to develop efficient electrical energy storage technology.^[1,5]

In this aspect, supercapacitors are the ideal choice for technologies that require fast charging and discharging, high power density, and long cycling stability. Supercapacitors can supply high power density, rapid charging, long cycle life ($>100\,000$ cycles), etc.^[6–8] However, the energy densities of batteries ($\approx 200 \text{ Wh Kg}^{-1}$) and fuel cells (up to 350 Wh Kg^{-1}) are superior to that of supercapacitors ($\approx 5 \text{ Wh Kg}^{-1}$) for most of the commercial supercapacitors.^[7,9] Hence, recent development of

S. R. Fernandes, R. S. Karmur, K. A. Padmalayam, N. N. Ghosh
Nano-materials Lab

Department of Chemistry
Birla Institute of Technology and Science
Pilani K K Birla Goa Campus, Goa 403726, India
E-mail: nghosh@goa.bits-pilani.ac.in

A. Maibam
ICGM
University of Montpellier
CNRS
ENSCM
34293 Montpellier, France

D. Hao
Centre for Atomaterials and Nanomanufacturing (CAN)
School of Science
RMIT University
Melbourne 3000, Australia

R. Babarao
Applied chemistry and environmental science

School of Science (STEM), and Centre for Advanced Materials & Industrial Chemistry (CAMIC) and ARC Centre of Excellence for Electrochemical Transformation of Carbon Dioxide

Department of Applied Chemistry and Environmental Science
School of Science
RMIT University
Melbourne, Victoria 3001, Australia

R. Babarao
Commonwealth Scientific and Industrial Research Organisation (CSIRO)
Normanby Road, Clayton, Victoria 3168, Australia

 Supporting information for this article is available on the WWW under <https://doi.org/10.1002/batt.202500466>

supercapacitors aims to overcome their low energy density value and makes them suitable for technologies that need high energy density as well as high power density.^[1,8,10,11] There are three types of supercapacitors, namely Electric-Double Layer Capacitors (EDLCs), Pseudocapacitors, and Hybrid capacitors. EDLC supercapacitors store charge electrostatically, and charge distribution occurs at the double-layer interfaces of electrode/electrolyte.^[1,10] EDLC materials possess high capacitance but limited energy density. Hence, the use of EDLC is restricted where a large amount of power is required to deliver over only a few seconds at a time. In pseudocapacitors, charge storage occurs because of the Faradic transfer of charges between electrodes and electrolytes. Pseudocapacitive materials offer greater specific capacitance and high energy densities. But due to low conductivity, sluggish diffusion, pseudocapacitive cycle life, inferior mechanical stability, and sometimes degrade at high potential.^[9–12] To achieve an energy storage device that can offer both high energy and high power, developing electrode materials by combining EDLC and pseudocapacitive materials could be a promising approach.^[1,10]

SCs are generally classified as symmetric supercapacitors and asymmetric supercapacitors (ASCs) based on the type of electrodes involved in the constructed device. In a symmetric type, both the positive and negative electrodes have the same electrode active material with equal weight. As water breakdown occurs at 1.23 V in aqueous electrolytes, symmetric supercapacitors often restrict the operating cell voltage, which severely limits the device's energy and power density.^[13] On the other hand, ASCs integrate two distinct positive and negative electrode active materials, which work in two different potential windows. Hence, ASCs operate at an extended potential window compared to symmetric SCs.^[1,14] The working potential window of ASCs can be extended up to \approx 2.0 V (for aqueous electrolytes), \approx 2.7 V (for organic electrolytes), and \approx 4.0 V (for ionic liquids). Aqueous electrolyte is mostly preferred because their ionic conductivity is higher, which enhances the power density of supercapacitors as well, and they are less expensive.^[1,15] The application of ionic and organic electrolytes is restricted as they are expensive, hydroscopic, need purification, in some cases are a fire hazard, etc.^[15]

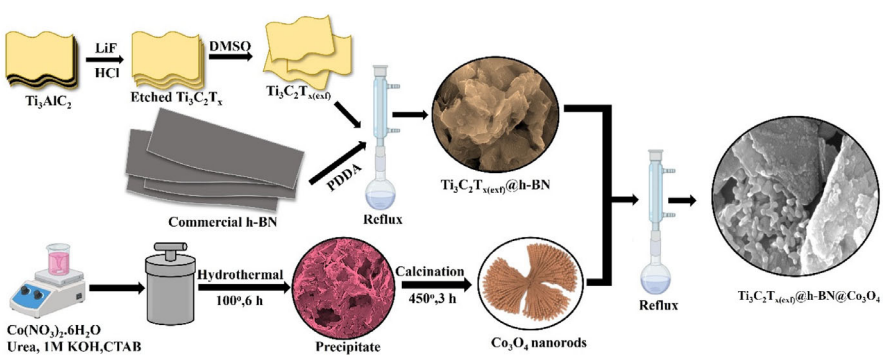
In the present work, for the cathode material of an ASC device, a hierarchical structure was created by combining

hexagonal boron nitride (h-BN), $\text{Ti}_3\text{C}_2\text{T}_{x(\text{exf})}$ MXene, and Co_3O_4 nanorods. h-BN exhibits rich electrochemical properties because of its sp^2 hybridization, presence of two electronegative atoms (C and N) with honeycomb arrangements, along with a layered structure, excellent mechanical strength, thermal and chemical stability, which are appropriate for an electrode material. However, the electrical conductivity of h-BN is poor. Hence, to improve the electrical conductivity of h-BN, it was combined with $\text{Ti}_3\text{C}_2\text{T}_{x(\text{exf})}$ MXene. MXenes are represented as $\text{M}_{n+1}\text{X}_n\text{T}_x$ (M = early transition metal, X denotes carbon (C) or nitrogen (N), and T_x = functional groups (-OH, -O, and -F) and $n = 1, 2, 3$, etc.).^[16–18] The existence of fascinating 2-D lamellar structures with ion transport channels, hydrophilic surface, abundant active sites for charge storage, high mechanical strength, exceptional metallic conductivity (\approx 6000–8000 S cm $^{-1}$) and presence of transition metal which can allow multiple oxidation states make MXenes a promising candidate for the application of an energy storage material.^[19,20]

Hence, integrating nanometre-thin highly conductive $\text{Ti}_3\text{C}_2\text{T}_{x(\text{exf})}$ MXene sheets with a 2-D layered structure of h-BN has been considered to obtain a highly active electrode material. On the surfaces of $\text{Ti}_3\text{C}_2\text{T}_{x(\text{exf})}$ @h-BN 2-D heterostructure, Co_3O_4 nanorods were immobilized to introduce more redox features to this heterostructure. In Co_3O_4 , with a spinel crystal structure, Co^{2+} ions occupy tetrahedral sites and Co^{3+} octahedral sites. The presence of Co^{2+} and Co^{3+} helps to facilitate Faradaic reactions. Moreover, the theoretical specific capacitance of Co_3O_4 is appreciably high (\approx 3560 F g $^{-1}$).^[21] However, in most cases, the reported value of Cs of Co_3O_4 varies from 300 to 1000 F g $^{-1}$. Here, Co_3O_4 with nanorod-like morphology was synthesized, anticipating that the nanorod-like structure might facilitate the charge transportation via the Ballistic charge transport mechanism. Hence, the heterostructure composed of $\text{Ti}_3\text{C}_2\text{T}_{x(\text{exf})}$ @h-BN@ Co_3O_4 holds promise to be a highly efficient cathode material for a high-performance asymmetrical supercapacitor.

2. Results and Discussion

To synthesize $\text{Ti}_3\text{C}_2\text{T}_{x(\text{exf})}$ @h-BN@ Co_3O_4 following steps were performed. Step 1: $\text{Ti}_3\text{C}_2\text{T}_x$ was synthesized from Ti_3AlC_2 MAX phase



Scheme 1. Schematic presentation of the synthesis process of $\text{Ti}_3\text{C}_2\text{T}_x$, $\text{Ti}_3\text{C}_2\text{T}_{x(\text{exf})}$, Co_3O_4 nanorods, $\text{Ti}_3\text{C}_2\text{T}_{x(\text{exf})}$ @h-BN, and $\text{Ti}_3\text{C}_2\text{T}_{x(\text{exf})}$ @h-BN@ Co_3O_4 heterostructure.

by removing its Al layer by the chemical etching technique. To obtain exfoliated $\text{Ti}_3\text{C}_2\text{T}_{x(\text{exf})}$, the layered structure of $\text{Ti}_3\text{C}_2\text{T}_x$ was exfoliated via intercalation with DMSO.^[16,22] Step 2: The surface of commercial h-BN was functionalized with PDDA, so that the negatively charged h-BN surface becomes positively charged. Step 3: The negatively charged $\text{Ti}_3\text{C}_2\text{T}_{x(\text{exf})}$ was self-assembled with positively charged h-BN by employing a reflux process, which resulted in the formation of $\text{Ti}_3\text{C}_2\text{T}_{x(\text{exf})}$ @h-BN (ζ potential = 51.58 mV). Step 4: Nanorod-shaped Co_3O_4 was synthesized by employing a hydrothermal method where $\text{Co}(\text{NO}_3)_2 \cdot 6\text{H}_2\text{O}$, Urea, KOH (1M), and Cetyltrimethylammonium Bromide (CTAB) were used as starting materials. The precipitate obtained after the hydrothermal process was calcined at 450 °C for 3 h, and thus, nanorod-shaped Co_3O_4 was obtained. The surface of the synthesized Co_3O_4 was negatively charged (ζ potential = -2 mV). Step 5: Finally, to synthesize $\text{Ti}_3\text{C}_2\text{T}_{x(\text{exf})}$ @h-BN@ Co_3O_4 heterostructure, the Co_3O_4 nanorods were immobilized on the surface and within the layers of $\text{Ti}_3\text{C}_2\text{T}_{x(\text{exf})}$ @h-BN by refluxing them together. In the final composition of this heterostructure, the wt% of $\text{Ti}_3\text{C}_2\text{T}_{x(\text{exf})}$, h-BN, and Co_3O_4 were 45%, 45%, and 10% respectively. The coulombic attraction between

the negatively charged Co_3O_4 and positively charged $\text{Ti}_3\text{C}_2\text{T}_{x(\text{exf})}$ @h-BN facilitates the formation of the $\text{Ti}_3\text{C}_2\text{T}_{x(\text{exf})}$ @h-BN@ Co_3O_4 heterostructure. Scheme 1 depicts the synthesis of $\text{Ti}_3\text{C}_2\text{T}_{x(\text{exf})}$ @h-BN@ Co_3O_4 . Porous carbon was synthesized from spent tea waste by treating it with concentrated H_2SO_4 , followed by a KOH activation technique.

The synthesized materials were characterized using powder X-ray diffraction (XRD), Raman spectroscopy, a Field Emission Scanning Electron microscope (FESEM), a High-Resolution Transmission Electron microscope (HRTEM), a ζ -potential analyzer, X-ray photoelectron spectroscopy (XPS), and Energy Dispersive X-ray spectroscopy (EDS).

The wide-angle powder X-ray diffraction (XRD) technique was used to identify the crystalline phases in the synthesized materials. The XRD patterns of the MAX phase (Ti_3AlC_2), MXene ($\text{Ti}_3\text{C}_2\text{T}_x$), and MXene_(exf) ($\text{Ti}_3\text{C}_2\text{T}_{x(\text{exf})}$) are presented in Figure 1a. Ti_3AlC_2 showed XRD peaks at $2\theta = 9.2, 18.7, 33.7, 34.8, 35.5, 36.4, 39.0, 41.4, 44.7, 48.2, 51.9, 56.1$ and 60.0° which can be ascribed to the (002), (004), (100), (101), (102), (103), (104), (105), (106), (107), (108), (109) and (110) diffraction planes [JCPDS card no. 52-0875] (Figure 1a). In the XRD pattern of $\text{Ti}_3\text{C}_2\text{T}_x$ which was

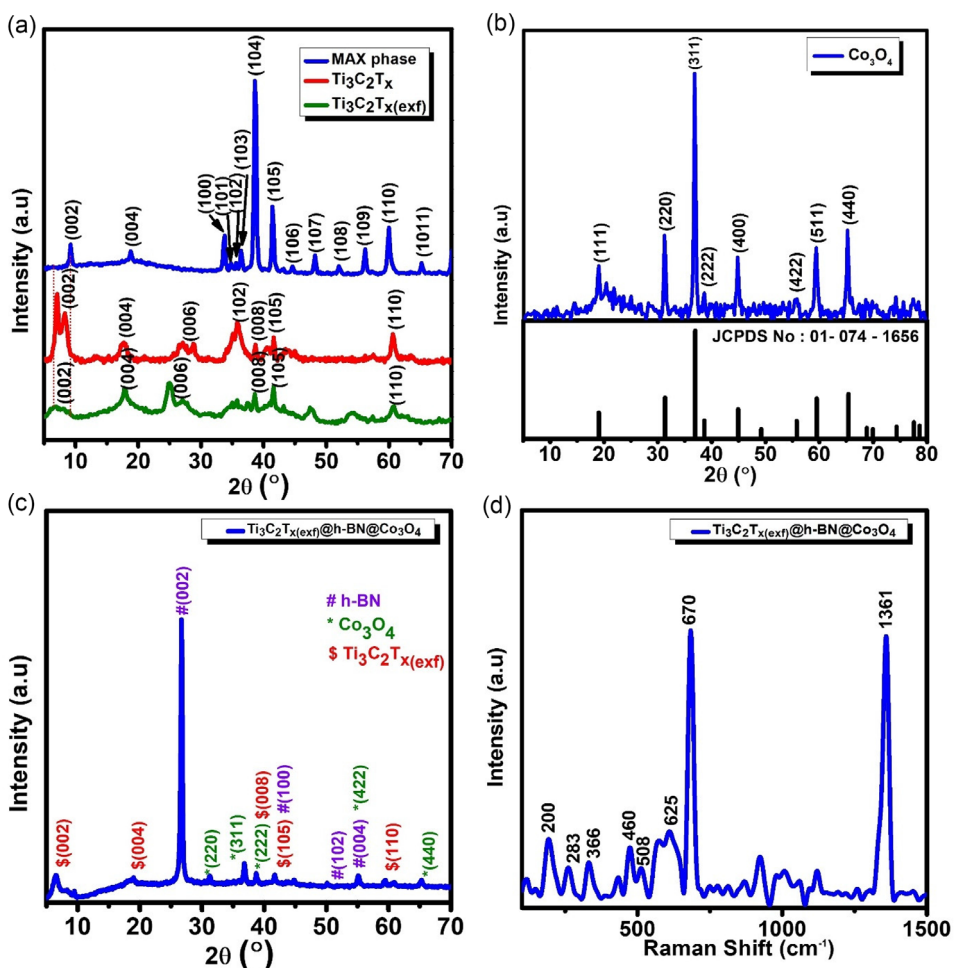


Figure 1. XRD pattern a) Ti_3AlC_2 (MAX phase), $\text{Ti}_3\text{C}_2\text{T}_x$ and $\text{Ti}_3\text{C}_2\text{T}_{x(\text{exf})}$, b) Co_3O_4 . c) $\text{Ti}_3\text{C}_2\text{T}_{x(\text{exf})}$ @h-BN@ Co_3O_4 and d) Raman spectra of $\text{Ti}_3\text{C}_2\text{T}_{x(\text{exf})}$ @h-BN@ Co_3O_4 .

obtained after Al layer etching from Ti_3AlC_2 showed peaks at $2\theta = 7.2, 18.0, 27.6, 35.7, 38.6, 41.5$, and 60.7° which correspond to (002), (004), (006), (102), (008), (105) and (110) diffraction planes (Figure 1a). It showed that the peak at $2\theta = 39.0^\circ$ has been diminished, indicating that the Al layer has been etched from Ti_3AlC_2 .^[23] Moreover, increase in the interlayer spacing because of the removal of the Al layer caused the broadening and shifting of the peak of (002) plane from $2\theta = 9.2^\circ$ ($d = 9.2 \text{ \AA}$) to $2\theta = 7.2^\circ$ ($d = 10.3 \text{ \AA}$) and also due to the -OH/ F^- groups on the surface of $\text{Ti}_3\text{C}_2\text{T}_x$.^[23] The exfoliated $\text{Ti}_3\text{C}_2\text{T}_{x(\text{exf})}$ which was obtained via intercalation of $\text{Ti}_3\text{C}_2\text{T}_x$ layers by DMSO displayed diffraction peaks at $2\theta = 6.7, 18.0, 27.6, 38.6, 41.5$, and 60.7° which correspond to its (002), (004), (006), (008), (105) and (110) diffraction planes (Figure 1a). Upon intercalation with DMSO, an increase in the interlayer spacing and exfoliation occurred, which was observed in the XRD pattern of $\text{Ti}_3\text{C}_2\text{T}_{x(\text{exf})}$. The XRD peak for (002) plane of $\text{Ti}_3\text{C}_2\text{T}_x$ ($2\theta = 7.2^\circ$, $d = 10.3 \text{ \AA}$) was shifted to $2\theta = 6.7^\circ$ ($d = 14.4 \text{ \AA}$)

and broadened in the XRD pattern of $\text{Ti}_3\text{C}_2\text{T}_{x(\text{exf})}$.^[19,24–27] This increase in the interlayer spacing confirms that the exfoliation of $\text{Ti}_3\text{C}_2\text{T}_x$ has taken place successfully.^[22] The diffraction plane (102) at $2\theta = 35.7^\circ$ which was observed in the XRD pattern of $\text{Ti}_3\text{C}_2\text{T}_x$ has now disappeared in the $\text{Ti}_3\text{C}_2\text{T}_{x(\text{exf})}$ due to the complete etching of the Ti_3AlC_2 MAX phase.^[26] Commercial hexagonal boron nitride (h-BN) in (Figure S1a, Supporting Information), displayed distinct diffraction peaks at $2\theta = 26.7, 41.5, 43.7, 50.1$, and 55.1° corresponding to its (002), (100), (101), (102), and (004) crystal planes respectively [JCPDS card no. 034-0421]. The XRD pattern of $\text{Ti}_3\text{C}_2\text{T}_{x(\text{exf})}$ @h-BN composite in Figure S1b, Supporting Information showed all the characteristic diffraction peaks of $\text{Ti}_3\text{C}_2\text{T}_{x(\text{exf})}$ and h-BN. The synthesized Co_3O_4 nanorods showed XRD peaks (Figure 1b) at $2\theta = 19, 31.2, 36.7, 38.5, 44.8, 55.7, 59.3$ and 65.2° which can be indexed to its (111), (220), (311), (222), (400), (422), (511) and (440) diffraction planes, respectively [JCPDS card no. 01-074-1656]. In the XRD pattern of

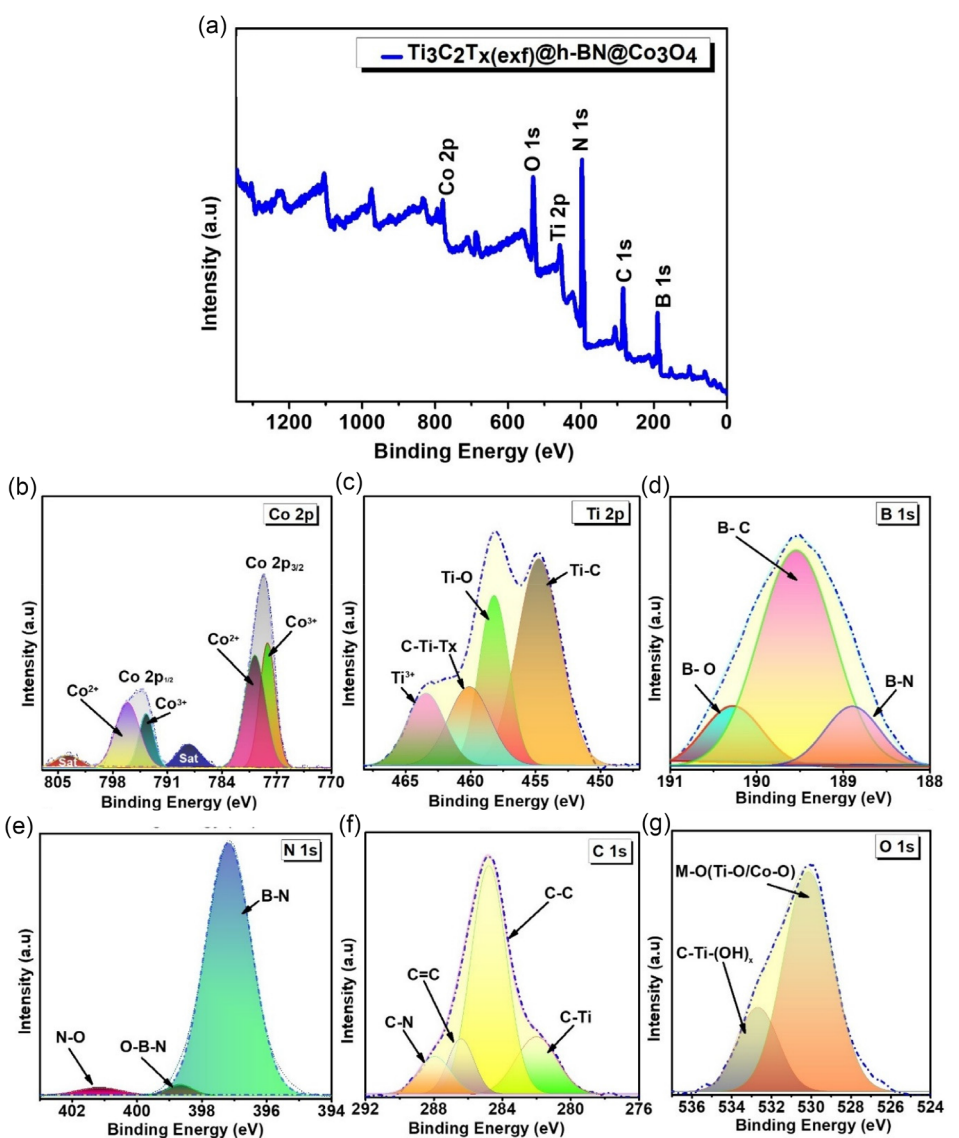


Figure 2. XPS spectra of $\text{Ti}_3\text{C}_2\text{T}_{x(\text{exf})}$ @h-BN@ Co_3O_4 a) Survey spectra b) Co 2p c) Ti 2p d) B 1s e) N 1s f) C 1s and g) O 1s.

$\text{Ti}_3\text{C}_2\text{T}_{x(\text{exf})}$ @h-BN@ Co_3O_4 heterostructure (Figure 1c), the presence of all the characteristic peaks of Co_3O_4 , $\text{Ti}_3\text{C}_2\text{T}_{x(\text{exf})}$, and h-BN was observed. In $\text{Ti}_3\text{C}_2\text{T}_{x(\text{exf})}$ @h-BN@ Co_3O_4 heterostructure, because of the exfoliation of $\text{Ti}_3\text{C}_2\text{T}_x$ layers and to some extend infusion of layers of 2D h-BN, the interplanar spacing of $\text{Ti}_3\text{C}_2\text{T}_x$ was increased which was reflected in the XRD pattern as the appearance of broad and split peak at $2\theta = 6\text{--}7^\circ$ for (002) plane of $\text{Ti}_3\text{C}_2\text{T}_{x(\text{exf})}$. This confirmed the successful formation of all three components (i.e., Co_3O_4 , $\text{Ti}_3\text{C}_2\text{T}_{x(\text{exf})}$, and h-BN) into the $\text{Ti}_3\text{C}_2\text{T}_{x(\text{exf})}$ @h-BN@ Co_3O_4 composite. The XRD pattern of porous carbon (Figure S1c, Supporting Information) displayed two broad humps, suggesting its amorphous nature. The peaks at around $2\theta = 22.8$ and 43.8° corresponded to (002) and (100) diffraction planes.^[28]

The high-resolution XPS technique was used to determine the chemical states of components in the $\text{Ti}_3\text{C}_2\text{T}_{x(\text{exf})}$ @h-BN@ Co_3O_4 heterostructure. The XPS survey spectrum presented in Figure 2a shows the existence of Co 2p, Ti 2p, B 1s, N1s, C1s, and O 1s. In the high-resolution spectra of Co 2p (Figure 2b), two major peaks were observed at 778.6 and 794.6 eV, which can be attributed to the $2p_{3/2}$ and $2p_{1/2}$, indicating that Co may exist in two valence states (Co^{2+} and Co^{3+}). The fitted peaks located at 778.1 and 793.6 eV correspond to Co^{3+} , while the peaks at 780.7 and 796.3 eV could be assigned to the Co^{2+} oxidation state.^[29,30] The satellite peaks were attained at 788.2 and 803.6 eV with an energy gap from the main peak of ≈ 9.3 eV, suggesting Co exists in its trivalent state. The XPS spectra of Ti 2p (Figure 2c) exhibited peaks at 454.7, 458.1, 460.2, and 463.4 eV, which correspond to Ti-C, Ti-O, C-Ti-T_x, and Ti³⁺.^[31,32] The B 1s spectra (Figure 2d) displayed signature peaks at 188.8, 189.4, and 190.2 eV corresponding to B-N, B-C, and B-O bonds, respectively. The peak that was obtained at 190.2 eV confirms the existence of oxygen functionality on the surface of boron nitride.^[33,34] The deconvolution of the N 1s spectrum in Figure 2e shows three peaks at 397.0, 398.6, and 401.0 eV, which can be ascribed to the B-N, O-B-N, and N-O bonds, respectively.^[34–36] After deconvoluting the C 1s XPS spectrum (Figure 2f), it was fitted into four peaks centered at 281.9, 284.7, 286.3, and 288.0 eV, which can be assigned to C-Ti, C-C, C=C, and C-N bonds, respectively.^[37,38] The O 1s spectra in Figure 2g displayed two peaks at 530.1 and 532.2 eV, which can be indexed to characteristic metal–oxygen bond (M-O, Co-O, Ti-O) and C-Ti-(OH)_x.^[39,40]

The Raman spectra of h-BN (Figure S2a, Supporting Information) showed a characteristic band at 1361 cm^{-1} , which represented the E_{2g} phonon mode analogous to the G peak observed in graphene.^[41] In the Raman spectra of Co_3O_4 (Figure S2b, Supporting Information), the vibration bands were observed at 189, 460, 508, 603, and 670 cm^{-1} .^[42] The band at 189 cm^{-1} could be assigned to its T_{2g} mode. The Raman bands located at 460 and 508 cm^{-1} correspond to the E_g and F_{2g}^1 symmetry, which are related to the combined vibrations and oxygen motions in the tetrahedral and octahedral sites.^[43] The band located at 603 cm^{-1} corresponds to the F_{2g}^2 symmetry. The strong Raman band appeared at 670 cm^{-1} was attributed to Co-O vibration due to Co^{3+} in the octahedral sites and assigned

to A_{1g} mode. All these modes are in agreement with the values of the pure Co_3O_4 spinel structure.^[44] The Raman spectra of $\text{Ti}_3\text{C}_2\text{T}_{x(\text{exf})}$ in Figure S2c, Supporting Information exhibited bands at 200, 244, 283, 366, 625, and 1371 cm^{-1} . The band at 200 cm^{-1} corresponds to the out-of-plane phonon mode of Ti, F/O/OH, C(ω_2). The peaks located at 244 and 366 cm^{-1} could be assigned to the in-plane (shear) modes of Ti, C, and surface terminal groups, respectively.^[45] The Raman bands that appeared at 283, and 625 cm^{-1} are due to the in-plane OH (ω_5) and in-plane C (ω_4) phonon modes.^[26] The presence of a band at 1371 cm^{-1} is due to the D band of Carbon in $\text{Ti}_3\text{C}_2\text{T}_x$.^[27] In the Raman spectra of $\text{Ti}_3\text{C}_2\text{T}_{x(\text{exf})}$ @h-BN@ Co_3O_4 heterostructure (Figure 1d), the characteristic Raman bands of Co_3O_4 , MXene(exf), and h-BN were observed. In the Porous carbon synthesized from spent tea waste, the bands were observed at 1342 and 1590 cm^{-1} which can be indexed to its D-band and G-bands (Figure S2d, Supporting Information).^[46] The D-band is caused due to the presence of defective carbon atoms, whereas the G-band arises due to the in-plane stretching of the symmetric sp^2 carbon atoms.

The microstructures of the synthesized materials were analysed by using FESEM and HRTEM as depicted in Figure 3. The FESEM micrograph of pure Co_3O_4 (Figure 3a) revealed its nanorod-like structure. These nanorods were formed via the conclave of nanoparticles and assembled to form a porous flower-like structure. $\text{Ti}_3\text{C}_2\text{T}_x$ (MXene), having a layered microstructure (Figure S3a, Supporting Information), was formed after etching the Al layer from Ti_3AlC_2 (MAX phase) (Figure S3b, Supporting Information). The exfoliation of the layers of $\text{Ti}_3\text{C}_2\text{T}_x$ ($\text{Ti}_3\text{C}_2\text{T}_{x(\text{exf})}$) was achieved through the intercalation of DMSO within the layers of $\text{Ti}_3\text{C}_2\text{T}_x$ (Figure 3e). Figure 3i shows the 2-D sheet-like microstructure of h-BN. Figure 3m reveals the microstructure of the $\text{Ti}_3\text{C}_2\text{T}_{x(\text{exf})}$ @h-BN@ Co_3O_4 heterostructure. It has been observed that a hierarchical structure has formed because of the infusion of nanosheets of $\text{Ti}_3\text{C}_2\text{T}_{x(\text{exf})}$ within the 2D layered structure of h-BN and the immobilization of Co_3O_4 nanospheres within and on the surface of their 2D heterostructure. The FESEM image of porous carbon is displayed in Figure S3c, Supporting Information, which shows its porous nature.^[47,48] The TEM micrographs displayed a round-shaped structure of Co_3O_4 (Figure 3b) and nanometre-thin layers of $\text{Ti}_3\text{C}_2\text{T}_{x(\text{exf})}$ (Figure 3f) and h-BN (Figure 3j). Figure 3n displays the TEM micrograph of $\text{Ti}_3\text{C}_2\text{T}_{x(\text{exf})}$ @h-BN@ Co_3O_4 , which divulges the intimate coexistence of the individual components from the heterostructure. The fringes were observed in the HRTEM microstructures of the synthesized materials. The fringes corresponding to (222), (111), and (400) planes ($d = 2.3, 4.6$, and 2.0 \AA), respectively, were observed for Co_3O_4 (Figure 3c). For $\text{Ti}_3\text{C}_2\text{T}_{x(\text{exf})}$, the fringes with d values 2.3 and 3.3 \AA were assigned to (008) and (006), respectively (Figure 3g). For h-BN, a fringe corresponding to the (002) plane with $d = 3.3\text{ \AA}$ was observed (Figure 3k). In the HRTEM micrograph of $\text{Ti}_3\text{C}_2\text{T}_{x(\text{exf})}$ @h-BN@ Co_3O_4 , the presence of fringes for Co_3O_4 ((222): $d = 2.4\text{ \AA}$), $\text{Ti}_3\text{C}_2\text{T}_{x(\text{exf})}$ ((002): $d = 3.4\text{ \AA}$) and h-BN ((006): $d = 3.3\text{ \AA}$) were observed (Figure 3o). The SAED patterns of Co_3O_4 , $\text{Ti}_3\text{C}_2\text{T}_{x(\text{exf})}$, h-BN, and $\text{Ti}_3\text{C}_2\text{T}_{x(\text{exf})}$ @h-BN@ Co_3O_4 composite are presented in Figure 3d,h,l,p. The spots observed for Co_3O_4 were indexed as (400) and (444) (Figure 3d), for $\text{Ti}_3\text{C}_2\text{T}_{x(\text{exf})}$ (004)

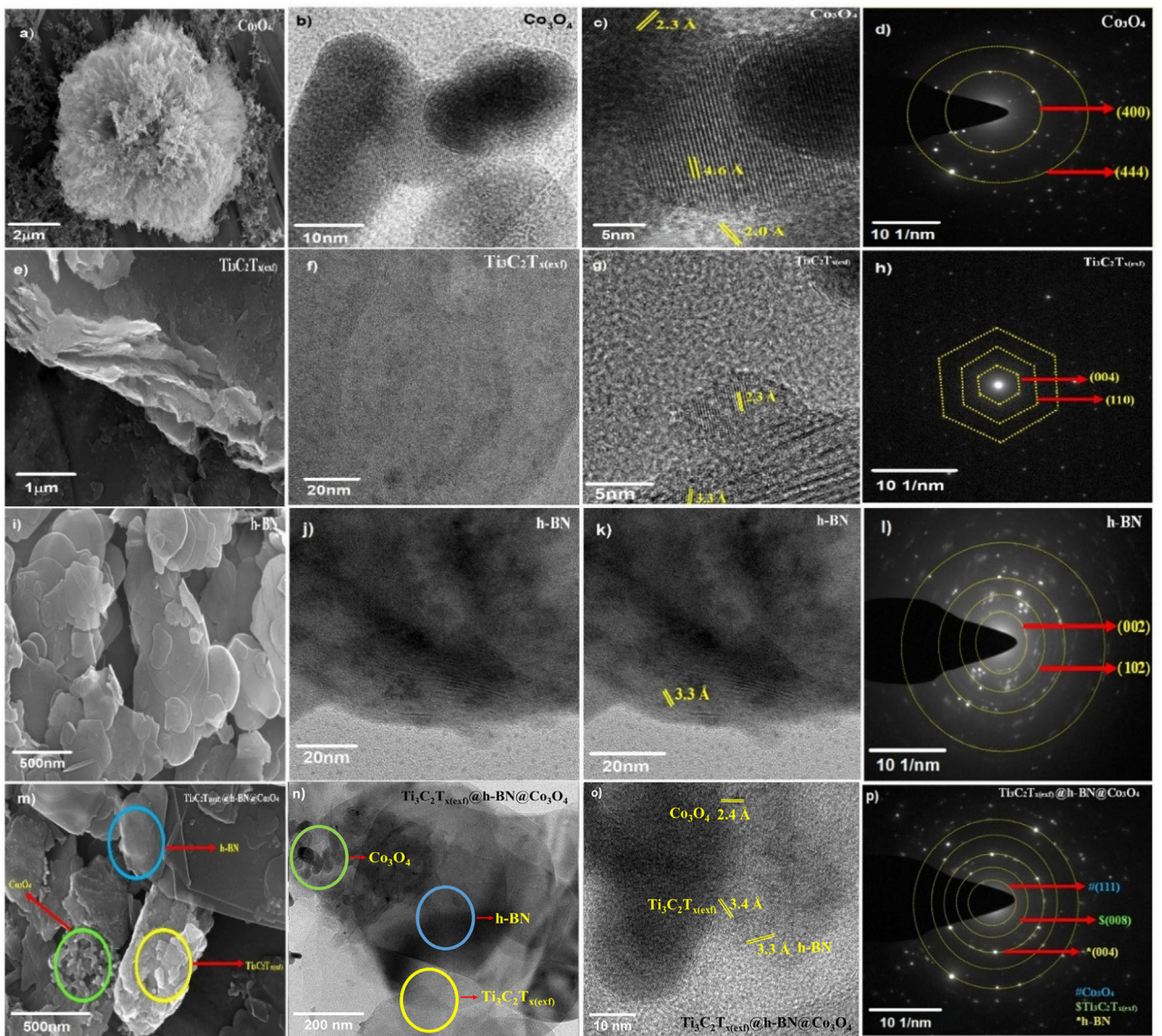
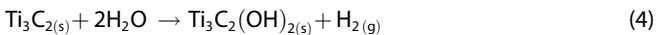
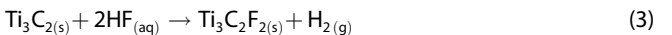


Figure 3. FESEM a,e,i,m) TEM b,f,j,n) HRTEM c,g,k,o) and SAED patterns d,h,l,p) of Co_3O_4 , $\text{Ti}_3\text{C}_2\text{T}_{x(\text{exf})}$, h-BN, and $\text{Ti}_3\text{C}_2\text{T}_{x(\text{exf})}@\text{h-BN}@\text{Co}_3\text{O}_4$.

and (100) (Figure 3h), and h-BN (002) and (102) (Figure 3l) crystallographic planes. In the SAED pattern of $\text{Ti}_3\text{C}_2\text{T}_{x(\text{exf})}@\text{h-BN}@\text{Co}_3\text{O}_4$, the observed spots were assigned to (111) planes of Co_3O_4 , (008) plane of $\text{Ti}_3\text{C}_2\text{T}_{x(\text{exf})}$, and (004) plane of h-BN (Figure 3p). Energy dispersive spectroscopy (EDS) confirmed the presence of all the elements (Figure S4a, Supporting Information). Moreover, Figure S5i, Supporting Information displays the STEM image, and Figure S5a–h, Supporting Information shows the elemental colour mapping of $\text{Ti}_3\text{C}_2\text{T}_{x(\text{exf})}@\text{h-BN}@\text{Co}_3\text{O}_4$ and confirms the presence of Co, B, N, Ti, C, O, and F uniformly in the heterostructure.

The aforesaid characterization techniques confirmed the formation of $\text{Ti}_3\text{C}_2\text{T}_{x(\text{exf})}$, Co_3O_4 nanorod, $\text{Ti}_3\text{C}_2\text{T}_{x(\text{exf})}@\text{h-BN}$, and $\text{Ti}_3\text{C}_2\text{T}_{x(\text{exf})}@\text{h-BN}@\text{Co}_3\text{O}_4$. During the synthesis of $\text{Ti}_3\text{C}_2\text{T}_x$ from Ti_3AlC_2 MAX phase via chemical etching using a mixture of LiF and HCl, the Al layer was removed from Ti_3AlC_2 , and a 2-D layer

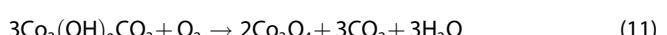
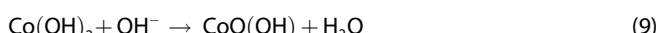
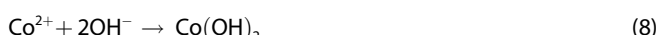
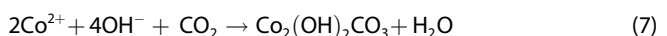
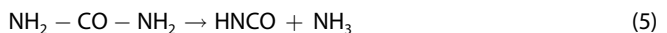
of $\text{Ti}_3\text{C}_2\text{T}_x$ was formed.^[13] The reactions which were involved in this synthesis can be presented as Equation (1)–(4).^[13] When $\text{Ti}_3\text{C}_2\text{T}_x$ was treated with DMSO, DMSO intercalated within the layers of $\text{Ti}_3\text{C}_2\text{T}_x$ and helped in the exfoliation process, which resulted in the formation of $\text{Ti}_3\text{C}_2\text{T}_{x(\text{exf})}$.^[49]



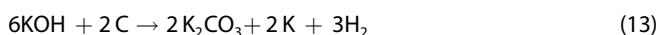
The formation of $\text{Ti}_3\text{C}_2\text{T}_{x(\text{exf})}@\text{h-BN}$ heterostructure was achieved via self-assembly of $\text{Ti}_3\text{C}_2\text{T}_{x(\text{exf})}$ and h-BN nanosheets.

To facilitate the self-assembly process, the surface charge of h-BN was altered. The ζ -potential value of $Ti_3C_2T_{x(exf)}$ was found to be -19.0 mV and h-BN was -38.30 mV . To obtain h-BN nanosheets with positive ζ -potential, the surface of h-BN was functionalized with PDDA, which made the ζ -potential of h-BN 69.45 mV . During the mixing process due to coulombic attraction, the negatively charged $Ti_3C_2T_{x(exf)}$ sheets and positively charged PDDA functionalized h-BN sheets were assembled and formed $Ti_3C_2T_{x(exf)}@h\text{-BN}$ (FESEM of $Ti_3C_2T_{x(exf)}@h\text{-BN}$ presented in Figure S6, Supporting Information). The ζ -potential of $Ti_3C_2T_{x(exf)}@h\text{-BN}$ was 51.75 mV .

To synthesize Co_3O_4 , a hydrothermal method was applied using an aqueous mixture of $Co(NO_3)_2\cdot 6H_2O$, Urea, KOH (1 M), and Cetyltrimethylammonium Bromide (CTAB).^[50] After hydrothermal treatment of this mixture, a light pink color precipitate was obtained. XRD measurement of this precipitate showed the presence of $Co(OH)_2$, $CoO(OH)$, and Co_3O_4 (Figure S7, Supporting Information). The reactions involved are presented as Equations (5)–(9). Its FESEM micrograph (Figure S8, Supporting Information) showed the presence of a mixture of thin flakes of irregular shape and some nanorod-shaped particles. The pink color precipitate after drying was calcined at $450\text{ }^\circ\text{C}$ for 3 h in air. This calcination process oxidized and decomposed the pink-colored precipitate (Equations (10)–(12)) and resulted in the formation of Co_3O_4 . Here, CTAB played the role of a structure-directing agent.^[51–53]

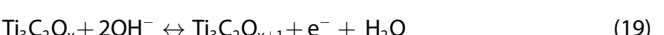


The negatively charged Co_3O_4 nanoparticles were immobilized on the surface and within the positively layered structure of $Ti_3C_2T_{x(exf)}@h\text{-BN}$ via a reflux method. The resulting $Ti_3C_2T_{x(exf)}@h\text{-BN}@Co_3O_4$ heterostructure possessed a positively charged surface (ζ -potential = 51.58 mV). (Intensity vs ζ -potential analysis plots are presented in Figure S9, Supporting Information). Porous Carbon (PC) was synthesized from the spent tea waste by treating it with concentrated H_2SO_4 , followed by potassium hydroxide activation. The reactions that were involved are presented in Equation (13)–(17).^[11,46]



To assess the potential of the synthesized materials as active electrode materials, electrochemical properties were determined by performing Cyclic Voltammetry (CV), Galvanostatic charge-discharge cycles (GCD), and Electrochemical Impedance spectroscopy (EIS) measurements in a three-electrode setup using an aqueous 3 M KOH electrolyte. CV measurements were performed in a potential window of $0\text{--}0.5\text{ V}$ (vs Ag/AgCl) with varying scan rates from 10 to 100 mV s^{-1} .

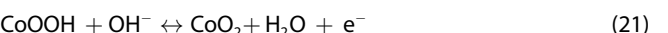
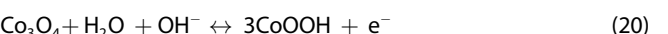
The pristine h-BN exhibited a pair of prominent oxidation-reduction peaks at $0.36\text{ V}/0.25\text{ V}$ (50 mVs^{-1}) (Figure S10a, Supporting Information). These redox peaks occur due to the transitioning oxidation states arising from its partial ionic character and might be due to the electronegativity difference between boron (2.04) and nitrogen (3.04).^[54] as well as from the reversible intercalation and deintercalation of electrolyte ions into and from the h-BN.^[55] GCD curves of h-BN indicated its pseudo-capacitance nature, and the specific capacitance (C_s) value of 191.7 Fg^{-1} was obtained at a current density of 1 Ag^{-1} (Figure S10b, Supporting Information). The Coulombic efficiency of h-BN was 85.5% . The layered structure and free π electrons in h-BN contributed to its charge storage capacity.^[56] In case of $Ti_3C_2T_x$ and $Ti_3C_2T_{x(exf)}$, the redox peaks were observed at $0.33\text{ V}/0.22\text{ V}$ and $0.35\text{ V}/0.22\text{ V}$ (50 mVs^{-1}), respectively (Figure S10c,e, Supporting Information). The alternating adsorption and desorption of OH^- ions on the surface of $Ti_3C_2T_x$ could be responsible for its pseudocapacitive behaviour, as given in Equation (18)–(19).^[57]



The larger area under the CV curve of $Ti_3C_2T_{x(exf)}$ than that of as-synthesized $Ti_3C_2T_x$ (unexfoliated) indicates the enhancement of C_s of $Ti_3C_2T_x$ due to exfoliation (Figure S11c, Supporting Information). The exfoliation might have made more active sites available and facilitated the intercalation between $Ti_3C_2T_x$ layers and $-\text{OH}$. The C_s values of the $Ti_3C_2T_x$ and $Ti_3C_2T_{x(exf)}$ obtained from GCD measurements are 109.8 and 172.6 Fg^{-1} (1 Ag^{-1}), respectively (Figure S10d,f, Supporting Information). An increase in Coulombic efficiency was observed because of the exfoliation of $Ti_3C_2T_x$. For unexfoliated $Ti_3C_2T_x$, Coulombic efficiency was 63.3% whereas for exfoliated $Ti_3C_2T_{x(exf)}$, it was 98% . The non-linear feature of the GCD curves indicated their pseudocapacitance nature.^[13] EIS measurement showed that the exfoliation caused a decrease in the charge transfer resistance (R_{CT}) of $Ti_3C_2T_{x(exf)}$. R_{CT} of unexfoliated $Ti_3C_2T_x$ and $Ti_3C_2T_{x(exf)}$ was 33.2 and 28.3Ω , respectively (Figure S11d and Table S1, Supporting Information). The lowering of R_{CT} of $Ti_3C_2T_{x(exf)}$ has resulted in the enhancement of conductivity and faster charge transfer kinetics, and might be responsible for its better electrochemical

performance. Because of better Cs, from now onwards, $\text{Ti}_3\text{C}_2\text{T}_{x(\text{exf})}$ was used to prepare different heterostructures. To enhance the electrochemical properties, a heterostructure was prepared by commingling $\text{Ti}_3\text{C}_2\text{T}_{x(\text{exf})}$ nanosheets with the layered structure of h-BN (50 : 50 wt%). The CV of $\text{Ti}_3\text{C}_2\text{T}_{x(\text{exf})}$ @h-BN exhibited redox peaks at 0.32/0.22 V (50 mVs⁻¹), demonstrating its pseudocapacitance nature (Figure S11a, Supporting Information). The area under the CV curve of $\text{Ti}_3\text{C}_2\text{T}_{x(\text{exf})}$ @h-BN was larger than that of $\text{Ti}_3\text{C}_2\text{T}_{x(\text{exf})}$ and h-BN (Figure S11c, Supporting Information). The Cs value (from GCD measurements (Figure S11b, Supporting Information) of $\text{Ti}_3\text{C}_2\text{T}_{x(\text{exf})}$ @h-BN was 259.5 Fg⁻¹ (1 Ag⁻¹), and this value was greater than that of its individual components. h-BN is semiconducting in nature, whereas $\text{Ti}_3\text{C}_2\text{T}_{x(\text{exf})}$ possesses semi-metallic features with faster charge transport ability. Having 2D layered structures, both these materials provide an easier charge transfer pathway. Integration of h-BN into $\text{Ti}_3\text{C}_2\text{T}_{x(\text{exf})}$ enhances the conductivity of $\text{Ti}_3\text{C}_2\text{T}_{x(\text{exf})}$ @h-BN, which plays a major role in achieving a larger Cs value. Hence, a synergistic effect arises in the heterostructure composed of $\text{Ti}_3\text{C}_2\text{T}_{x(\text{exf})}$ and h-BN. Table S2, Supporting Information lists the Cs value of different compositions of $\text{Ti}_3\text{C}_2\text{T}_{x(\text{exf})}$ and h-BN. It was observed that the composite having 50 wt% $\text{Ti}_3\text{C}_2\text{T}_{x(\text{exf})}$ and 50 wt% h-BN showed the highest Cs value of 259.5 Fg⁻¹ at 1 Ag⁻¹. Hence, this composition was chosen to integrate with Co_3O_4 . Now onwards, this composition will be referred to as $\text{Ti}_3\text{C}_2\text{T}_{x(\text{exf})}$ @h-BN. EIS measurements showed

that because of the integration of $\text{Ti}_3\text{C}_2\text{T}_{x(\text{exf})}$, the R_{CT} of h-BN (86.2 Ω) (Figure S11d and Table S1, Supporting Information) has decreased significantly. The R_{CT} of $\text{Ti}_3\text{C}_2\text{T}_{x(\text{exf})}$ @h-BN was 40.9 Ω. For further enhancement of the electrochemical properties of $\text{Ti}_3\text{C}_2\text{T}_{x(\text{exf})}$ @h-BN, Co_3O_4 nanoparticles were immobilized on the surface of the layers. The CV scan of pure Co_3O_4 is presented in Figure S10g, Supporting Information, which showed a pair of distinct redox peaks at 0.35/0.20 V (50 mVs⁻¹) which could be attributed to the change of oxidation states (2+, 3+, and 4+) during redox reaction in the aqueous solution of KOH (Equations (20) and (21)).^[58–60] These reversible reactions can be summarised as follows



From the GCD measurements, the Cs of Co_3O_4 was determined as 377.7 Fg⁻¹ at 1 Ag⁻¹ (Figure S10h, Supporting Information), and its Coulombic efficiency was 99.05 %. The nature of CV profiles and GCD curves suggests the pseudocapacitance nature of Co_3O_4 . EIS measurements exhibited the R_{CT} of Co_3O_4 as 17 Ω.

The CV curve of this $\text{Ti}_3\text{C}_2\text{T}_{x(\text{exf})}$ @h-BN@ Co_3O_4 has been presented in Figure 4a, which shows the presence of redox peaks at 0.34/0.23 V (50 mVs⁻¹), and the area under the CV curve

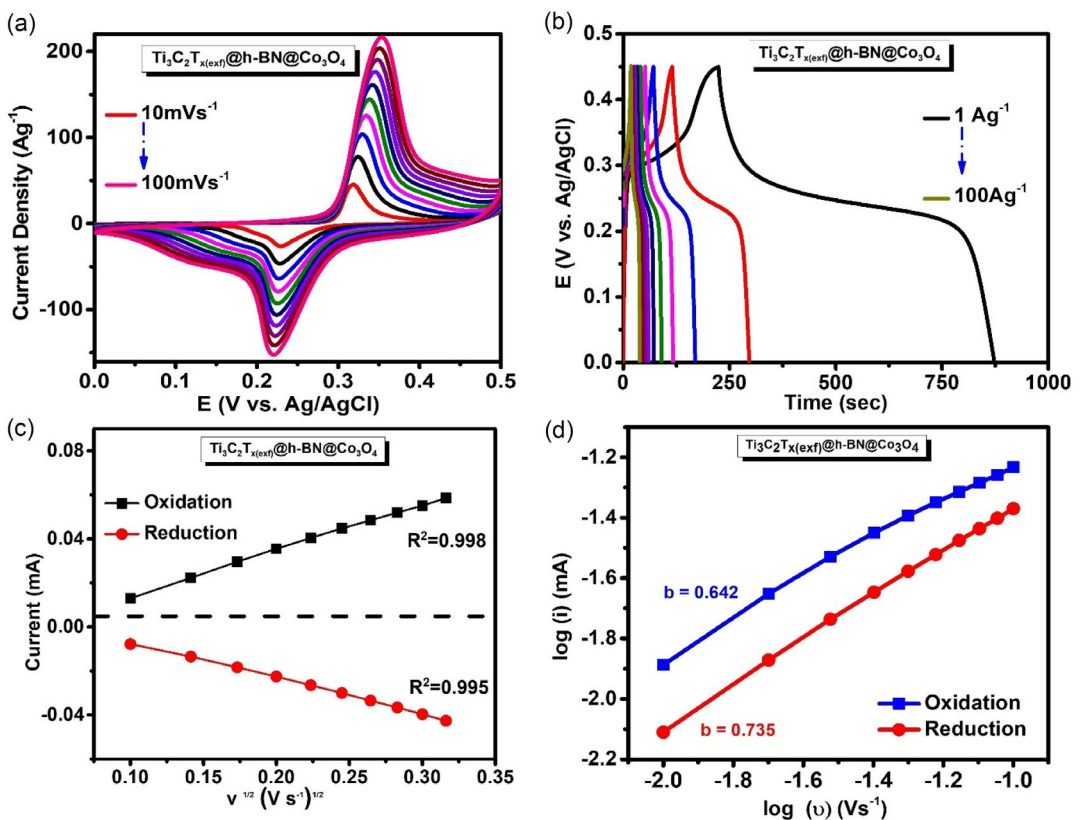


Figure 4. a) CV profile at various scan rates, b) GCD profile at different current densities, c) Randles-Sevcik plot, and d) log i vs. log v plot of $\text{Ti}_3\text{C}_2\text{T}_{x(\text{exf})}$ @h-BN@ Co_3O_4 heterostructure.

was significantly larger than that of pure $\text{Ti}_3\text{C}_2\text{T}_{\text{x(exf)}}$, h-BN, and $\text{Ti}_3\text{C}_2\text{T}_{\text{x(exf)}}@\text{h-BN}$ (Figure S11c, Supporting Information). The shapes of CV and GCD curves indicated the pseudocapacitance nature of $\text{Ti}_3\text{C}_2\text{T}_{\text{x(exf)}}@\text{h-BN}@\text{Co}_3\text{O}_4$. The C_s value of this heterostructure obtained from GCD was 922 Fg^{-1} at 1 Ag^{-1} (Figure 4b), and the Coulombic efficiency was 87.9%. In Table S3, Supporting Information, the C_s values of different compositions of $\text{Ti}_3\text{C}_2\text{T}_{\text{x(exf)}}@\text{h-BN}@\text{Co}_3\text{O}_4$ are listed. The composition with 45 wt% $\text{Ti}_3\text{C}_2\text{T}_{\text{x(exf)}}$, 45 wt% h-BN, and 10 wt% Co_3O_4 displayed the highest C_s value. Here onwards, this composition has been referred to as $\text{Ti}_3\text{C}_2\text{T}_{\text{x(exf)}}@\text{h-BN}@\text{Co}_3\text{O}_4$. Because of the complex heterostructure as well as the presence of three electroactive materials in $\text{Ti}_3\text{C}_2\text{T}_{\text{x(exf)}}@\text{h-BN}@\text{Co}_3\text{O}_4$, its charge-discharge profile deviated from linearity.^[61] When CV measurements were performed at different scan rates (Figure 4a), it was observed that the oxidation and reduction peaks were shifted to the positive and negative directions, respectively, with increasing scan rate, which suggested the development of overpotentials that limit the redox reaction.^[62] A well-linear increasing trend of the peak current with increasing scan rate (as shown in the Randles-Sevcik plot (Figure 4c)), suggested the diffusion-controlled nature of the redox process, which occurred on the electrode surface, and a good rate capability of this heterostructure. To understand the charge storage mechanism, $\log i$ vs $\log v$ ($i = av^b$, i is the current response, v is the scan rate, and a and b are adjustable parameters) was plotted (Figure 4d). The values of slope b were 0.642 (anodic) and 0.735 (cathodic), which suggested that a diffusion-controlled process, as well as an electrochemical process, contribute to the charge storage mechanism of $\text{Ti}_3\text{C}_2\text{T}_{\text{x(exf)}}@\text{h-BN}@\text{Co}_3\text{O}_4$. EIS measurements (Figure S11d, Supporting Information)

revealed that the R_{CT} value of this heterostructure was 0.17Ω , which was lower than pure $\text{Ti}_3\text{C}_2\text{T}_{\text{x(exf)}}$, h-BN, and $\text{Ti}_3\text{C}_2\text{T}_{\text{x(exf)}}@\text{h-BN}$. These results indicated the enhanced electrochemical property of $\text{Ti}_3\text{C}_2\text{T}_{\text{x(exf)}}@\text{h-BN}@\text{Co}_3\text{O}_4$, and hence, here we used it to prepare the cathode for an asymmetric supercapacitor device. Our previous studies demonstrated that porous carbon (PC) derived from spent tea is an efficient anode material.^[28] The CV and GCD curves of PC, in the potential window of -1 to 0 V , are shown in Figure S12a,b, Supporting Information. The almost rectangular shape of CV curves and linear GCD plots suggests the EDLC nature of PC in this potential window in aqueous KOH electrolyte. The porous structure of PC facilitates the adsorption of -OH on its surface. The value of C_s for PC was 440.6 Fg^{-1} at 1 A g^{-1} , which was determined from GCD measurement (Figure S12b, Supporting Information). EIS measurement shows the R_{CT} value of PC was 1.9Ω (Figure S12c, Supporting Information). PC was used as an active anode material to construct an asymmetrical supercapacitor.

A 2-E asymmetric configuration was constructed using $\text{Ti}_3\text{C}_2\text{T}_{\text{x(exf)}}@\text{h-BN}@\text{Co}_3\text{O}_4$ as the cathode, PC as the anode, and a filter paper as a separator, which was soaked with 3 M KOH electrolyte aqueous solution. The CV profiles of $\text{Ti}_3\text{C}_2\text{T}_{\text{x(exf)}}@\text{h-BN}@\text{Co}_3\text{O}_4$ and, PC (obtained from 3-E setup) were found to be stable in 0 to 0.5 V and -1 to 0 V potential window, respectively (Figure 5b). Hence, for this ASC device (2-E setup $\text{Ti}_3\text{C}_2\text{T}_{\text{x(exf)}}@\text{h-BN}@\text{Co}_3\text{O}_4/\text{PC}$), CV was measured at different potential windows, and a stable working potential window was found as 0 – 1.5 V (Figure 5b). On operating this device at 1.6 V , a distortion in the CV and GCD profile (circled in red) was observed, which could be due to the thermodynamic

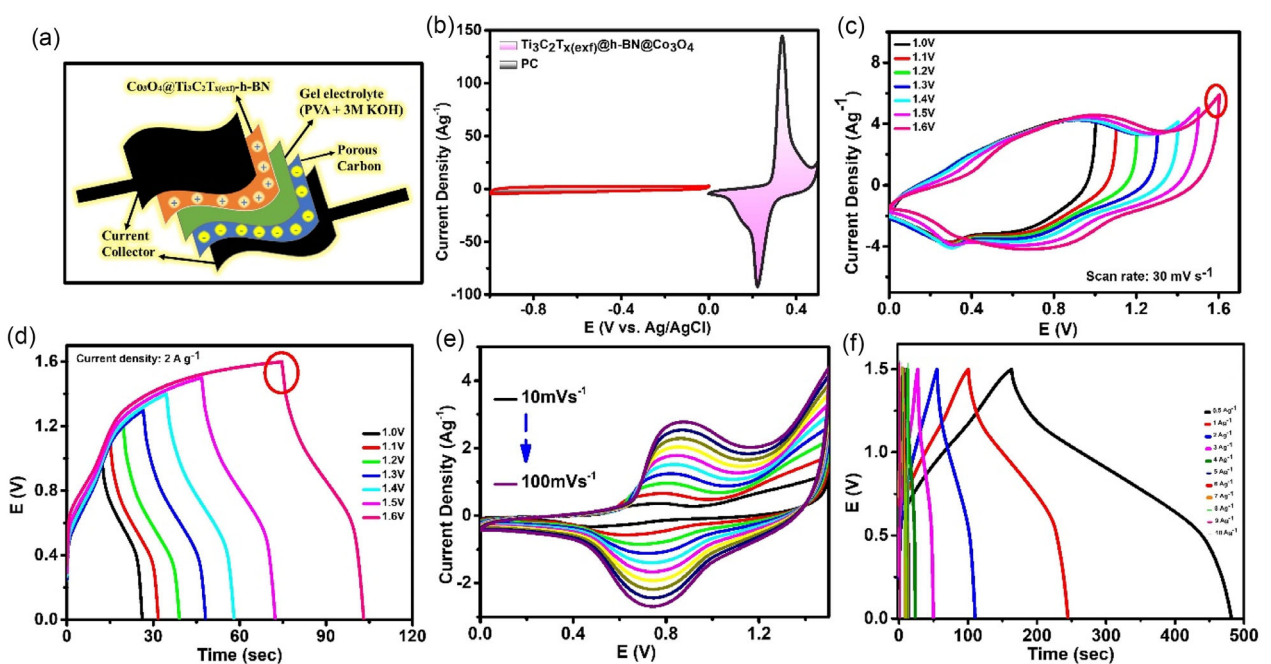


Figure 5. a) Descriptive diagram of assembled solid-state ASC device ($\text{Ti}_3\text{C}_2\text{T}_{\text{x(exf)}}@\text{h-BN}@\text{Co}_3\text{O}_4/\text{PC}$) using Gel electrolyte cum separator (PVA + 3 M KOH), b) CV curves of positive electrode (0 to 0.5 V), and negative electrode (-1 to 0 V), c) CV curves and d) GCD curves of ASC device with different potential windows. e) CV profile with various scan rates and f) GCD profile with various current densities for the ASC device.

breakdown of water (Figure S13a and S1, Supporting Information).^[27] CV was performed at various scan rates as depicted in Figure S13c, Supporting Information. This device demonstrated almost symmetrical-shaped GCD profiles from current density of 0.5 to 9 Ag⁻¹ (Figure S13d, Supporting Information). The specific capacitance (C_s) value of the device was 142.0 F g⁻¹ at a current density of 0.5 A g⁻¹. In the $\text{Ti}_3\text{C}_2\text{T}_{x(\text{exf})}\text{@h-BN@Co}_3\text{O}_4/\text{PC}$ asymmetric supercapacitor device, the complex hierarchical structure and composition of cathode and anode, as well as the difference between their charging-discharging rates, affect the device's charge-discharge process, which results in the difference in the charging-discharging time. This device delivered an energy density of 44.3 Wh Kg⁻¹ at a power density of 375 W kg⁻¹. Based on the EIS measurements from the Nyquist plot, the R_S and R_{CT} were calculated to be 0.2 and 0.2 Ω. $\text{Ti}_3\text{C}_2\text{T}_{x(\text{exf})}\text{@h-BN@Co}_3\text{O}_4/\text{PC}$ all-solid-state ASC device was now assembled by using PVA-KOH (gel-electrolyte) as presented in Figure 5a. Here, the polymer gel containing Polyvinyl alcohol (PVA) and 3 M KOH acted as both the separator as well as an electrolyte to make an all-solid-state ASC device. The appropriate operating voltage window for this device was optimized from 0 to 1.5 V by performing CV and GCD (Figure 5c,d). The CV measurements at the scan rates of 10 to 100 mVs⁻¹ showed uniformity, signifying the device's excellent rate capability (Figure 5e). The C_s value obtained from GCD measurement of this ASC device (Figure 5f), was 105.8 F g⁻¹ at a current density of 0.5 A g⁻¹, and the energy density value was obtained as 33.0 Wh kg⁻¹ at a power density of 375 W kg⁻¹. A Ragone plot (Energy density vs Power density) is presented in Figure 6a,

which illustrates the performance of $\text{Ti}_3\text{C}_2\text{T}_{x(\text{exf})}\text{@h-BN@Co}_3\text{O}_4/\text{PC}$ compared with the reported ASC devices, which were prepared by using a similar type of material and is presented in Table S4, Supporting Information.^[55,63-71] The electrochemical performances of $\text{Ti}_3\text{C}_2\text{T}_{x(\text{exf})}\text{@h-BN@Co}_3\text{O}_4/\text{PC}$ were found to be similar and, in some cases, superior to many reported results. The mechanical flexibility of the $\text{Ti}_3\text{C}_2\text{T}_{x(\text{exf})}\text{@h-BN@Co}_3\text{O}_4/\text{PC}$ solid-state ASC device was assessed by performing CV at various bending angles like 0°, 90°, and 180°, and twisting form (Figure 6b), from which not much change in the CV curve was observed. To evaluate the life span of this device, 5000 charge-discharge cycles were carried out at 5 A g⁻¹, and the device could retain ≈90% of its initial capacitance and ≈85% of its Coulombic efficiency, hence demonstrating excellent long-term durability (Figure 6c). From the Nyquist plot, R_{CT} and R_S values were determined as 0.38 and 0.68 Ω, respectively. This indicates the lower resistance and shows faster charge transfer in this device. For lab-scale applications, LEDs were illuminated using this solid-state ASC device, thereby serving as a source of power. Figure 6d illustrates four solid-state $\text{Ti}_3\text{C}_2\text{T}_{x(\text{exf})}\text{@h-BN@Co}_3\text{O}_4/\text{PC}$ devices were connected in series and successfully powered a series of 16 LEDs. This lab-scale demonstration proves the potential of this device for practical use as a flexible energy storage device.

To gain an in-depth understanding of the hierarchical electrode material, $\text{Ti}_3\text{C}_2\text{T}_{x(\text{exf})}\text{@h-BN@Co}_3\text{O}_4$ computational investigations were first carried out on the individual h-BN, Ti_3C_2 and Co_3O_4 components. Pristine h-BN nanosheet has been modelled as B25N25geometry and the optimized structure showed a standard

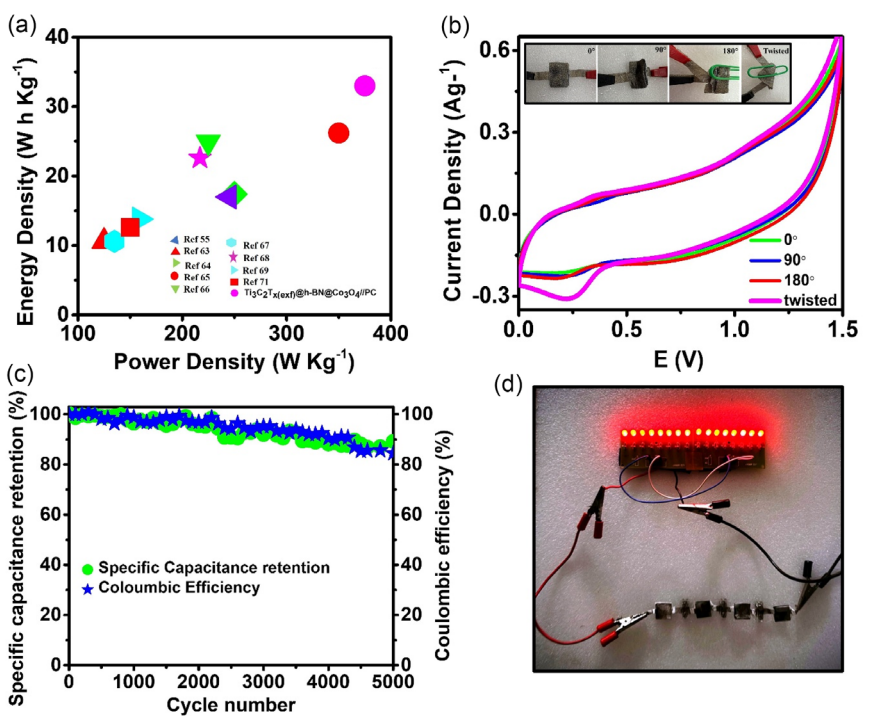


Figure 6. a) Ragone plot, b) CV profiles at different angles, c) Cyclic stability test upto ≈5000 GCD cycles and Coulombic efficiency, and d) snap of a panel of 16 LEDs illuminated by 4 devices in a series connection.

B-N bond length of 1.43 Å, bond angle of 120° and band gap of 4.6 eV as depicted in Figure S14a, Supporting Information. These structural parameters match reasonably well with previously obtained experimental results^[72] while the computed excess surface charge density maxima of $-14.93 \mu\text{Ccm}^{-2}$ at -1 V and maximum quantum capacitance of $16.84 \mu\text{Fcm}^{-2}$ observed at -0.96 V electrode potential (Figure S15, Supporting Information) is in close agreement to previously reported theoretical values of Σ and C_q on a B16N16 model of h-BN.^[73] The relatively lower values of Σ and C_q in h-BN are in direct correspondence to the suppression of the density of states at the Fermi level, and the material shows a prominent band gap and semiconducting nature. Ti₃C₂ nanosheet and Co₃O₄ nanoparticles, on the other hand, are conducting with enhanced density of states (DOS) near the Fermi level, thereby these two components show zero band gap, Figure S14b,c, Supporting Information, and relatively higher Σ and C_q values (Figure S16, Supporting Information). Interestingly, Ti₃C₂ being a highly conductive material with enhanced density of states in the valence and conduction region, shows a higher quantum capacitance maximum of $65.52 \mu\text{Fcm}^{-2}$ at -2.88 V , while Co₃O₄ nanoparticle with sparsely populated density of states in the conducting region attributes to a maximum C_q of $22.62 \mu\text{Fcm}^{-2}$ at -1.46 V electrode potential.

Integrating these conductive materials with h-BN leads to a significant increase in the Σ and C_q values as the Fermi region becomes populated and enhanced, Figure S14d,e, Supporting Information. The enhanced electron density near the Fermi level of Ti₃C₂@h-BN and Ti₃C₂@Co₃O₄ signifies that these electrodes are more conducting than the individual components. A detailed analysis from the projected density of states (PDOS) in Figure 7a,b shows a higher intensity of Ti d-orbitals in Ti₃C₂@h-BN, while in Ti₃C₂@Co₃O₄, both Ti d-orbitals and Co d-orbitals show a higher electronic density; thereby, the conductive nature is mostly attributed to the metal d-orbitals. Figure 7c,d shows the variation in excessive surface charge density (Σ) and quantum capacitance (C_q) of Ti₃C₂@h-BN and Ti₃C₂@Co₃O₄ with respect to the electrode potential. It was observed that C_q maximum of Ti₃C₂@h-BN was $55.48 \mu\text{Fcm}^{-2}$ at -2.67 V (negative bias), while the highest C_q for Ti₃C₂@h-BN@Co₃O₄ was $59.16 \mu\text{Fcm}^{-2}$ at 2.67 V (positive bias), whereas the corresponding C_q maximum for Ti₃C₂@h-BN at this positive bias potential was $48.55 \mu\text{Fcm}^{-2}$. The additional contribution from Co d-orbitals in the projected density of states explains the improvement in the conductive nature of the material. Furthermore, with the introduction of Co₃O₄, Co d-orbitals are made available in the conduction region, inferring that the empty

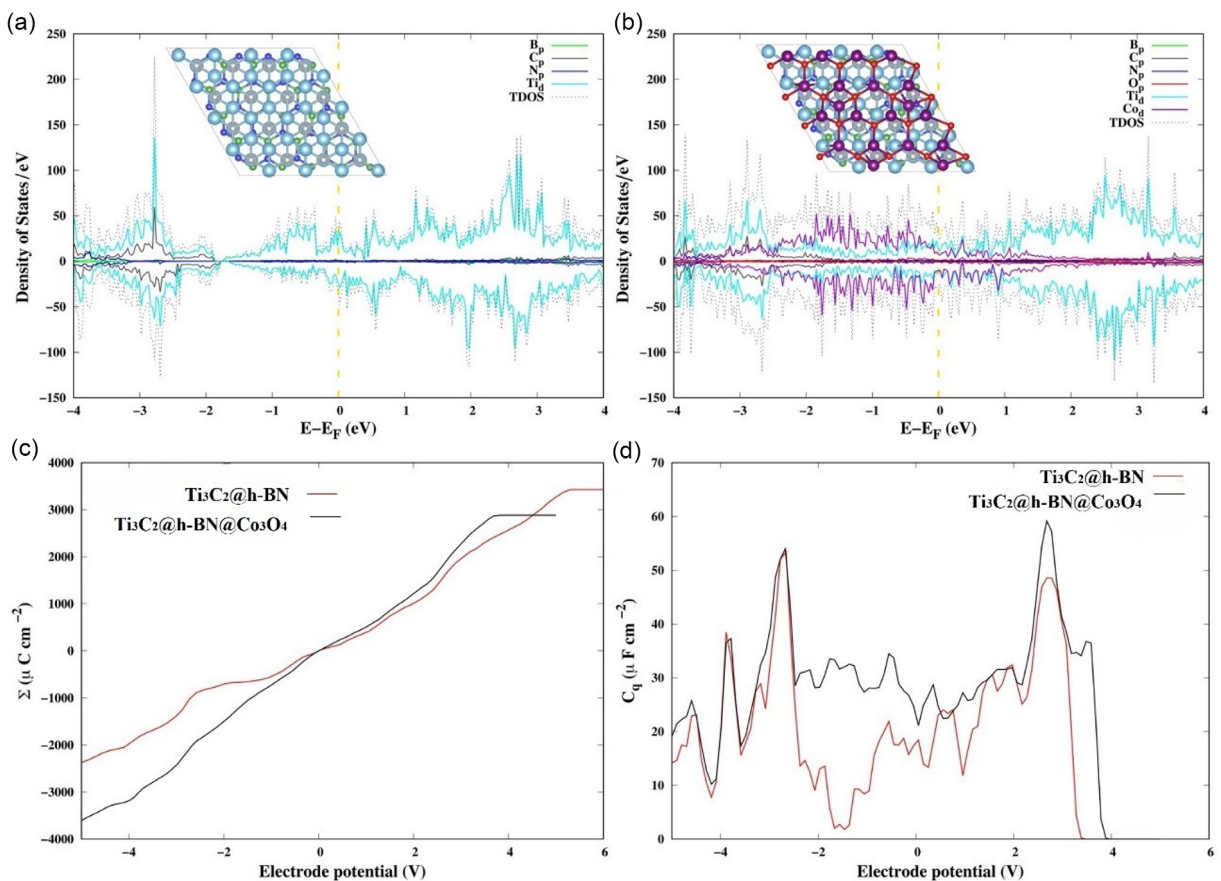


Figure 7. Projected density of states (PDOS) plots showing contribution from different elements with an inset showing a model top view of a) Ti₃C₂@h-BN, b) Ti₃C₂@h-BN@Co₃O₄. Variation in c) excessive surface charge density (Σ) and d) quantum capacitance (C_q) of Ti₃C₂@h-BN (red line) and Ti₃C₂@h-BN@Co₃O₄ (black line) with electrode potential. (Atomic colour codes : B (green), C(grey), N (blue), O(red), Ti (cyan), Co (violet).

Co d-orbitals will be accessible for storing charges, leading to better supercapacitor performance of $\text{Ti}_3\text{C}_2@\text{h-BN}@\text{Co}_3\text{O}_4$ as compared to $\text{Ti}_3\text{C}_2@\text{h-BN}$.

3. Conclusion

In this work, we successfully prepared a hierarchical heterostructure ($\text{Ti}_3\text{C}_2\text{T}_{x(\text{exf})}@\text{h-BN}@\text{Co}_3\text{O}_4$) by combining exfoliated $\text{Ti}_3\text{C}_2\text{T}_{x(\text{exf})}$ nanosheets with 2-D h-BN layered structure, followed by immobilizing Co_3O_4 nanorods on the surface of this structure. A flexible asymmetric supercapacitor was made using $\text{Ti}_3\text{C}_2\text{T}_{x(\text{exf})}@\text{h-BN}@\text{Co}_3\text{O}_4$ as cathode, a spent tea-derived porous carbon (PC) as anode, and PVA-KOH as gel-electrolyte cum separator. This $\text{Ti}_3\text{C}_2\text{T}_{x(\text{exf})}@\text{h-BN}@\text{Co}_3\text{O}_4//\text{PC}$ device showed a specific capacitance of 105.8 F g^{-1} at a current density of 0.5 A g^{-1} . Its energy density was 33.0 W h kg^{-1} at a power density of 375 W kg^{-1} . It also exhibited retention of $\approx 90\%$ of its initial capacitance and $\approx 85\%$ of its Coulombic efficiency after 5000 charge-discharge cycles. This device also demonstrated its mechanical flexibility by delivering similar electrochemical performance even at various bending angles. DFT calculations revealed the comparison in the electronic density of the states between $\text{Ti}_3\text{C}_2\text{T}_{x(\text{exf})}@\text{h-BN}@\text{Co}_3\text{O}_4$ and the individual components, and their values of excessive surface charge density and quantum capacitance. The highest quantum capacitance for $\text{Ti}_3\text{C}_2\text{T}_{x(\text{exf})}@\text{h-BN}@\text{Co}_3\text{O}_4$ was obtained as $59.16 \mu\text{F cm}^{-2}$ at 2.67 V (positive bias). The illumination of LEDs by the $\text{Ti}_3\text{C}_2\text{T}_{x(\text{exf})}@\text{h-BN}@\text{Co}_3\text{O}_4//\text{PC}$ ASC device indicated its application in high-performing flexible all-solid-state supercapacitor devices. This work sheds light on the prospect of the application of MXene-based heterostructures in state-of-the-art energy storage devices.

4. Experimental Section

Materials

Cobalt Nitrate hexahydrate ($\text{Co}(\text{NO}_3)_2 \cdot 6\text{H}_2\text{O}$), Ti_3AlC_2 MAX phase (particle size $\leq 200 \mu\text{m}$), Lithium Fluoride (LiF), Boron Nitride Nanopowder APS 70 nm, Poly(diallyldimethylammonium chloride) (PDDA), Polyvinylidene difluoride (PVDF), acetylene black, N-methyl-2-pyrrolidinone (NMP), polyvinyl alcohol (PVA), Poly(diallyldimethylammonium chloride) (PDDA). Hydrochloric acid (HCl) and Urea ($\text{CO}(\text{NH}_2)_2$) were purchased from Merck, India. Potassium Hydroxide (KOH) was purchased from Fisher Scientific. Ni foam was purchased from Hi-Tech Scientific Equipment, Kolkata, India. Deionized water (DI water) was used during the experiments.

Materials Preparation: Synthesis of Co_3O_4 Nanorods

In the first step, $\text{Co}(\text{NO}_3)_2 \cdot 6\text{H}_2\text{O}$ (9 mM), Urea (0.08 mM), and Cetyltrimethylammonium bromide (CTAB) (0.001 mM) were stirred for 30 min, and its pH was adjusted to $\approx 7-8$ using 1 M KOH. This mixture was autoclaved in a Teflon vessel for 6 h at 100°C . The obtained product was washed and dried thoroughly, and later calcined for 3 h at 450°C to obtain these nanorods.

Materials Preparation: Synthesis of $\text{Ti}_3\text{C}_2\text{T}_{x(\text{exf})}$

Ti_3AlC_2 is the MAX phase precursor from which the Al layer is etched to synthesize MXene $\text{Ti}_3\text{C}_2\text{T}_x$ nanosheets by using LiF/HCl chemical etchant. The etchant was prepared by adding 0.5 g LiF in 10 mL of 9 M HCl solution and continuously stirring it to dissolve the LiF powder. To it 0.5 g of Ti_3AlC_2 MAX precursor powder was gradually added and then magnetically stirred at room temperature for 48 h. The product was collected by centrifuging, washing with distilled water, and the washing was continued until the pH value of the supernatant came to around ≥ 5 . MXene powder was obtained after drying at 60°C for 12 h. Later, the obtained $\text{Ti}_3\text{C}_2\text{T}_x$ (100mg) was exfoliated in 25 mL DMSO by magnetically stirring (300–400 RPM) it for 24h, followed by sonication for 1 h. It was centrifuged and washed using deionized water and oven-dried at 60°C for 12 h to obtain $\text{Ti}_3\text{C}_2\text{T}_{x(\text{exf})}$.

Materials Preparation: Synthesis of Porous Carbon

The spent tea waste was washed and dried under sunlight for 24 h. In a Teflon-lined autoclave, 2 g of this tea waste, about 50 mL of concentrated H_2SO_4 were added and heated at 200°C for 24 h. The obtained black product was washed with water until $\approx \text{pH } 7$ and dried at 60°C to obtain porous carbon precursor. Solid crushed KOH and the precursor (1:1 wt%) were ground and mixed well using a mortar and pestle, and this mixture was calcinated at 850°C for 3 h in N_2 atmosphere in a tube furnace. The obtained product was then washed with water till $\approx \text{pH } 7$ and dried at 60°C for 12 h to obtain porous carbon (PC).^[28] Commercial h-BN Nanopowder was used for the preparation of composites in this further study.

Materials Preparation: Characterization of Materials

For the characterization of synthesized materials were employed by using the following characterization techniques: i) Field emission scanning electron microscopy (FESEM) images of materials were attained using Quanta 250 FEG (FEI), ii) High-resolution transmission electron microscopy (HRTEM) and selected area electron diffraction (SAED) images were obtained by HR-TEM 200 kV JEOL JEM-F200, iii) Energy dispersive X-Ray spectra (EDS) and elemental mapping was obtained from EDAX ELEMENT electron microscope attached to a Quanta 250 FEG (FEI), iv) X-Ray diffraction (XRD) patterns of the prepared materials were carried out using a powder X-Ray diffractometer (Mini Flex II, Rigaku, Japan) with Cu K α ($\lambda = 0.15405 \text{ nm}$) radiation at a scanning speed of 3° min^{-1} , v) Zeta Potential was measured using Nanoparticle Analyzer of make Anton Paar (Model : Litesizer 500) vi) Raman spectra were recorded on a Horiba via Raman microscope with a 532 nm laser excitation, vii) XPS measurements were recorded using a Thermo-Scientific K-Alpha X-Ray photoelectron spectrometer having a monochromatic Al K α X-Ray source (1486.6 eV) and hemispherical energy analyzer. AUTOLAB PGSTAT204 Potentiostat workstation was used to perform the electrochemical studies.

Electrochemical Characterization: Three Electrode (3-E) Setup

Electrochemical tests were performed (CV, GCD, and EIS measurements) in a 3 electrode (3-E) cell setup. An Ag/AgCl double-junction electrode, a platinum wire, and Ni foam coated with the active material were used as the reference, counter, and working electrode to construct the three-electrode configuration, respectively. Electrochemical measurements were conducted by performing cyclic voltammetry (CV) and galvanostatic charge-discharge (GCD) in the potential window of 0 to 0.5 V for $\text{Ti}_3\text{C}_2\text{T}_x$, $\text{Ti}_3\text{C}_2\text{T}_{x(\text{exf})}$, h-BN, Co_3O_4 , $\text{Ti}_3\text{C}_2\text{T}_{x(\text{exf})}@\text{h-BN}$, and $\text{Ti}_3\text{C}_2\text{T}_{x(\text{exf})}@\text{h-BN}@\text{Co}_3\text{O}_4$.

h-BN@Co₃O₄. Electrochemical impedance spectroscopy (EIS) measurements were performed from 0.01 to 10 000 Hz with an alternating current amplitude of 5 mV. Ti₃C₂T_{x(exf)}@h-BN@Co₃O₄ was used as the cathode, and porous carbon (synthesized from spent tea waste) was used as the anode material to construct the flexible all-solid-state asymmetric supercapacitor device. The CV and GCD measurements for Porous Carbon were performed in the potential window of -1 to 0 V.

Electrochemical Characterization: Two-Electrode (2-E) Assembly

An ASC device was fabricated using a 2E-cell setup, with Ti₃C₂T_{x(exf)}@h-BN@Co₃O₄ as the cathode and porous carbon as the anode. A Whatman filter paper soaked in aqueous 3M KOH was used as an electrolyte cum separator. The positive and negative electrode mass ratio was optimized using a theory of charge balance ($q_+ = q_-$). In this Ti₃C₂T_{x(exf)}@h-BN@Co₃O₄/PC ASC device, the mass ratio (m^+/m^-) was ≈ 0.9 .

Electrochemical Characterization: All-Solid-State ASC Device

To fabricate a solid-state ASC device, PVA-KOH electrolyte was used. To prepare PVA-KOH, 30 mL of distilled water was heated on a hot plate. 1.0 g KOH was added to the boiling water, which is followed by the slow addition of 2.0 g Polyvinyl Alcohol, and stirred until it attains a gel-like texture. This gel was then pasted between the positive and negative electrodes. It was then kept for drying at room temperature for 12 h.

Electrochemical Characterization: Electrode Preparation

The working electrode was fabricated by preparing a viscous paste of active electrode material (80 wt%) with poly(vinylidene fluoride) (10 wt%) in N-methyl-2-pyrrolidinone and acetylene black. This paste was further coated onto the nickel foam (1.5 cm × 1.5 cm) and dried at 60 °C for 24 h under vacuum to remove the traces of solvent. Mass loading on the nickel foam ≈ 1.5 mg. For ASC cell only one side of the Nickel foam was coated.

The voltametric charges (Q) were calculated using the equations (Equation (22))

$$Q = C_{\text{single}} \times \Delta V \times m \quad (22)$$

where C_{single} is the specific capacitance (Fg⁻¹) of each electrode measured in a three-electrode setup (calculated from galvanostatic charge-discharge cycle at 1Ag⁻¹), ΔV is the potential window, and m is the mass (g) of the electrode.

The specific capacitance (C_s) values for the three-electrode as well as the two-electrode asymmetric cells were determined by using Equation (23)

$$C_s = \frac{i\Delta t}{m\Delta V} \quad (23)$$

where i is the charge or the discharge current in Ampere (A), Δt is the discharge time in seconds (s), m represents the mass of supercapacitor material in gram (g), and ΔV is the applied potential window.

For the 2E cell study, the charge/mass ratio for both cathode and anode were determined by using the Equation (24)

$$\frac{q_+}{q_-} = \frac{m_+}{m_-} = \frac{C_{\text{sp}}^+}{C_{\text{sp}}^-} \times \frac{\Delta V^-}{\Delta V^+} \quad (24)$$

Where C_{sp}^+ is the specific capacitance value obtained for the cathode material in the potential window ΔV^+ and C_{sp}^- is the specific capacitance value obtained for the anode material in the potential window ΔV^- . The Energy density (E) and Power density (P) for a two-electrode setup were calculated by using the following Equation (25) and (26)

$$E = \int_{t1}^{t2} IV(t) dt \times \frac{1000}{3600} \quad (25)$$

$$P = \frac{E}{\Delta t} \times 3600 \quad (26)$$

Where E is the energy density (W h kg⁻¹), and P is the power density (W kg⁻¹).

The Coulombic efficiency (η) was determined by using the following Equation (27)

$$\eta (\%) = \frac{t_d}{t_c} \times 100 \quad (27)$$

Where t_d and t_c are the discharging and charging times, respectively.

Electrochemical Characterization: Computational Details

Density functional theory (DFT) calculations were performed on a model hexagonal boron nitride (h-BN) nanosheet, a Ti₃C₂ MXene layer, and a Co₃O₄ (311) plane using density functional theory (DFT) as implemented in the Vienna ab initio simulation package (VASP).^[74,75] A generalized gradient approximation (GGA) method was employed with the Perdew-Burke-Ernzerhof (PBE) exchange correlation to define the ion-electron interaction of the electrons defined using the projector augmented wave (PAW) method.^[76] An energy cutoff of 400 eV was applied, with a k-point mesh of $3 \times 3 \times 1$ for geometry optimization with the van der Waals forces accounted by the Grimme DFT-D3 method.^[77] A vacuum spacer of 20 Å was inserted along the z-direction to avoid interlayer interactions. For the geometry optimization calculations, the atomic positions were relaxed until the total energy was converged to 1×10^{-5} eV and the Hellman-Feynman force on each relaxed atom was less than -0.03 eV Å⁻¹. Linear tetrahedral smearing techniques were used to integrate the Brillouin zone for density of states calculations with a Monkhorst-Pack scheme sampled at $11 \times 11 \times 1$ along the x, y, and z directions. The band structure calculations were made along the Γ --M--K--- Γ high symmetry first Brillouin zone path. In the design of the electrode materials, the electronic density of states at the Fermi level plays a crucial role for evaluating the potential of electronic charge accumulation expressed as excessive surface charge density (Σ) and quantum capacitance (C_q).

The excessive surface charge density (Σ) can be evaluated from the density of states (DOS) using Equation (28).^[78]

$$\Sigma = e \int_{-\infty}^{\infty} \text{DOS}(E)[f(E) - f(E - e\varphi)]dE \quad (28)$$

where e is the elementary electric charge, DOS(E) is the density of states of the material, $f(E) = \frac{1}{1 + \exp(\frac{E}{k_B T})}$ is the Fermi-Dirac distribution function, E is the energy relative to the Fermi energy level (EF), φ is the local electrochemical potential of the material, k_B is the Boltzmann constant, and $T = 300$ K is the temperature in standard conditions. The quantum capacitance, C_q is defined by the variation

of local charge density with respect to the potential and is expressed in an analytical form as stated in Equation (29).^[78]

$$C_q = \frac{d \sum}{d\varphi} = e^2 \int_{-\infty}^{\infty} DOS(E) F_T(E - e\varphi) dE \quad (29)$$

where $F_T(E)$ is a thermal broadening function defined as, $F_T(E) = (4kT) / (2e^2 h^2) E / (2kT)$.

Acknowledgements

N.N.G. and S.R.F. acknowledge the Cross-Disciplinary Research Framework (CDRF) scheme, BITS Pilani (Grant: C1/23/121), for financial support. The authors thank the Department of Biotechnology (DBT), India, DBT-BUILDER (Grant: BT/INF/22/SP42543/2021) for financial assistance and the XPS facility. The authors thank the Central Sophisticated Instrumentation Facility (CSIF), BITS Pilani K K Birla Goa Campus, for providing Zeta potential, Raman spectroscopy, FESEM, HRTEM, and EDX elemental mapping facilities. R.B. acknowledges the National Computing Infrastructure (NCI), Australia, for providing the computational resources.

Conflict of Interest

The authors declare no conflict of interest.

Author Contributions

Sarifa Regina Fernandes: investigation, conceptualization, methodology, data curation, writing—original draft, writing review and editing. **Rajeshvari Samatbhai Karmur:** methodology, experimentation, software, validation, conceptualization. **Krishna Aravind Padmalayam:** conceptualization, formatting review and editing. **Derek Hao:** Editing of the manuscript. **Ashakiran Maibam:** DFT calculation analysis, writing review and editing, and data curation. **Ravichandar Babarao:** resources, supervision, writing review and editing. **Narendra Nath Ghosh:** resources, funding acquisition, supervision, data curation, writing—review and editing.

Data Availability Statement

The data that support the findings of this study are available from the corresponding author upon reasonable request.

Keywords: asymmetric supercapacitor · cobalt oxide nanorods · density functional theory · density of states · hexagonal boron nitride · quantum capacitance · $Ti_3C_2T_x$

- [1] S. Sharma, P. Chand, *Results Chem.* **2023**, *5*, 100885.
- [2] C. H. Gebara, A. Laurent, *Renew. Sust. Energ.* **2023**, *173*, 112934.
- [3] J. He, Y. Yang, Z. Liao, A. Xu, K. Fang, *Appl. Energy* **2022**, *317*, 119167.
- [4] N. Abas, A. Kalair, N. Khan, *Futures* **2015**, *69*, 31.

- [5] C. Day, G. Day, *Econ. Model.* **2017**, *63*, 153.
- [6] M. E. Şahin, F. Blaabjerg, A. Sangwongwanich, *Energies* **2022**, *15*, 674.
- [7] Y. Shao, M. F. El-Kady, J. Sun, Y. Li, Q. Zhang, M. Zhu, H. Wang, B. Dunn, R. B. Kaner, *Chem. Rev.* **2018**, *118*, 9233.
- [8] W. Raza, F. Ali, N. Raza, Y. Luo, K. H. Kim, J. Yang, S. Kumar, A. Mahmood, E. E. Kwon, *Nano Energy* **2018**, *52*, 441.
- [9] J. Ding, H. Wang, Z. Li, K. Cui, D. Karpuzov, X. Tan, A. Kohandehghan, D. Mitlin, *Energy Environ. Sci.* **2015**, *8*, 941.
- [10] N. Kumar, S. Bin Kim, S. Y. Lee, S. J. Park, *Nanomater.* **2022**, *12*, 3708.
- [11] R. S. Karmur, D. Gogoi, M. R. Das, N. Nath Ghosh, *Chem. Asian J.* **2025**, *20*, e202401711.
- [12] H. Wang, H. S. Casalongue, Y. Liang, H. Dai, *J. Am. Chem. Soc.* **2010**, *132*, 7472.
- [13] R. S. Karmur, D. Gogoi, M. R. Das, N. N. Ghosh, *Energ. Fuel* **2022**, *36*, 8488.
- [14] R. Suresh, K. Tamilarasan, D. Senthil Vadivu, *Orient J Chem.* **2018**, *34*, 3058.
- [15] C. Zhong, Y. Deng, W. Hu, J. Qiao, L. Zhang, J. Zhang, *Chem. Soc. Rev.* **2015**, *44*, 7484.
- [16] M. Naguib, M. Kurtoglu, V. Presser, J. Lu, J. Niu, M. Heon, L. Hultman, Y. Gogotsi, M. W. Barsoum, *Adv. Mater.* **2011**, *23*, 4248.
- [17] Y. Wang, B. Zhou, Q. Tang, Y. Yang, B. Pu, J. Bai, J. Xu, Q. Feng, Y. Liu, W. Yang, *Adv. Mater.* **2024**, *36*, 2410736.
- [18] Y. Wang, N. Chen, B. Zhou, X. Zhou, B. Pu, J. Bai, Q. Tang, Y. Liu, W. Yang, *Nanomicro. Lett.* **2023**, *15*, 231.
- [19] R. S. Karmur, D. Gogoi, A. Biswas, C. Prathibha, M. R. Das, N. N. Ghosh, *Appl. Surf. Sci.* **2023**, *623*, 157042.
- [20] P. Zhang, J. Li, D. Yang, R. A. Soomro, B. Xu, *Adv. Funct. Mater.* **2023**, *33*, 2209918.
- [21] X. Zhou, X. Shen, Z. Xia, Z. Zhang, J. Li, Y. Ma, Y. Qu, *ACS Appl. Mater. Interfaces* **2015**, *7*, 20322.
- [22] A. Tsyganov, M. Vikulova, D. Artyukhov, D. Zhelezov, A. Gorokhovsky, N. Gorshkov, *Nanomater.* **2023**, *13*, 1337.
- [23] H. Fang, Y. Pan, M. Yin, C. Pan, *J. Mater. Sci.: Mater. Electron.* **2019**, *30*, 14954.
- [24] A. Iakunkov, N. Boulanger, B. Gurzeda, G. Li, C. Hennig, V. Svitlyk, M. R. V. Jørgensen, I. Kantor, I. A. Baburin, M. M. Hamed, A. V. Talyzin, *Chem. Mater.* **2025**, *37*, 1132.
- [25] S. Munir, A. Rasheed, T. Rasheed, I. Ayman, S. Ajmal, A. Rehman, I. Shakir, P. O. Agboola, M. F. Warsi, *ACS Omega* **2020**, *5*, 26845.
- [26] S. Adomaviciute-Grabusove, A. Popov, S. Ramanavicius, V. Sablinskas, K. Shevchuk, O. Gogotsi, I. Baginskiy, Y. Gogotsi, A. Ramanavicius, *ACS Nano* **2024**, *18*, 13184.
- [27] D. Gogoi, R. S. Karmur, M. R. Das, N. N. Ghosh, *J. Mater. Chem. A. Mater.* **2023**, *11*, 23867.
- [28] D. Gogoi, R. S. Karmur, M. R. Das, N. N. Ghosh, *Energ. Fuel.* **2023**, *37*, 14350.
- [29] J. Si, S. Xiao, Y. Wang, L. Zhu, X. Xia, Z. Huang, Y. Gao, *Nanoscale* **2018**, *10*, 2596.
- [30] R. Zhang, Y. Lu, L. Wei, Z. Fang, C. Lu, Y. Ni, Z. Xu, S. Tao, P. Li, *J. Mater. Sci.: Mater. Electron.* **2015**, *26*, 9941.
- [31] X. Wang, N. Han, Y. Zhang, G. Shi, Y. Zhang, D. Li, *J. Mater. Sci.: Mater. Electron.* **2022**, *33*, 21091.
- [32] S. A. Shah, T. Habib, H. Gao, P. Gao, W. Sun, M. J. Green, M. Radovic, *ChemComm* **2017**, *53*, 400.
- [33] R. Zhu, Q. Tao, M. Lian, X. Feng, J. Liu, M. Ye, X. Wang, S. Dong, T. Cui, P. Zhu, *Materials* **2019**, *12*, 1780.
- [34] C. K. Maity, S. Sahoo, K. Verma, G. C. Nayak, *Energ. Fuel* **2022**, *36*, 2248.
- [35] H. Sediri, D. Pierucci, M. Hajlaoui, H. Henck, G. Patriarche, Y. J. Dappe, S. Yuan, B. Toury, R. Belkhoud, M. G. Silly, F. Sirotti, M. Boutchich, A. Ouerghi, *Sci. Rep.* **2015**, *5*, 16465.
- [36] S. H. Lee, H. Jeong, O. F. N. Okello, S. Xiao, S. Moon, D. Y. Kim, G. Y. Kim, J. I. Lo, Y. C. Peng, B. M. Cheng, H. Miyake, S. Y. Choi, J. K. Kim, *Sci. Rep.* **2019**, *9*, 10590.
- [37] N. Li, C. Wang, L. Chen, C. Ye, Y. Peng, *Molecules* **2022**, *27*, 6732.
- [38] S. Zhang, W. Lu, C. Wang, Q. Shen, L. Zhang, *Appl. Phys. Lett.* **2012**, *101*, 141602.
- [39] V. Natu, M. Benchakar, C. Canaff, A. Habrioux, S. Célérrier, M. W. Barsoum, *Cell Press* **2021**, *4*, 1224.
- [40] R. S. Karmur, D. A. Upadhyay, Z. Mei, D. Hao, C. Liu, N. N. Ghosh, *Energ. Fuels* **2025**, *39*, 2854.
- [41] C. Gautam, S. Chelliah, *RSC Adv.* **2021**, *11*, 31284.
- [42] X. J. Zhou, P. H. Shi, Y. F. Qin, J. C. Fan, Y. L. Min, W. F. Yao, *J. Mater. Sci.: Mater. Electron.* **2016**, *27*, 1020.
- [43] A. Diallo, A. C. Beye, T. B. Doyle, E. Park, M. Maaza, *Green Chem. Lett. Rev.* **2015**, *8*, 30.

- [44] S. Farhadi, M. Javanmard, G. Nadri, *Acta. Chim. Slov.* **2016**, *63*, 335.
- [45] Y. Y. Yang, W. T. Zhou, W. L. Song, Q. Q. Zhu, H. J. Xiong, Y. Zhang, S. Cheng, P. F. Luo, Y. W. Lu, *Nanoscale Res. Lett.* **2021**, *16*, 60.
- [46] D. Gogoi, P. Makkar, M. R. Das, N. N. Ghosh, *ACS Appl. Electron. Mater.* **2022**, *4*, 795.
- [47] M. Fu, W. Chen, J. Ding, X. Zhu, Q. Liu, *J. Alloys Compd.* **2019**, *782*, 952.
- [48] H. J. Peng, G. X. Hao, Z. H. Chu, Y. W. Lin, X. M. Lin, Y. P. Cai, *RSC Adv.* **2017**, *7*, 34104.
- [49] G. Lv, J. Wang, Z. Shi, L. Fan, *Mater. Lett.* **2018**, *219*, 45.
- [50] N. K. Yetim, *J. Mol. Struct.* **2021**, *1226*, 129414.
- [51] X. Han, Z. Huang, C. He, Q. Zhang, X. Zhang, Y. Yang, *J. Appl. Electrochem.* **2019**, *49*, 1133.
- [52] M. M. Durano, A. H. Tamboli, H. Kim, *Colloids Surf. Physicochem. Eng. Asp.* **2017**, *520*, 355.
- [53] R. Lakra, R. Kumar, D. Nath Thatoi, P. Kumar Sahoo, A. Soam, *Mater. Today Proc.* **2021**, *41*, 269.
- [54] S. Kumari, A. Chouhan, O. P. Sharma, S. A. Tawfik, M. J. S. Spencer, S. K. Bhargava, S. Walia, A. Ray, O. P. Khatri, *ACS Appl. Nano Mater.* **2021**, *4*, 9143.
- [55] T. Li, X. Jiao, T. You, F. Dai, P. Zhang, F. Yu, L. Hu, L. Ding, L. Zhang, Z. Wen, Y. Wu, *Ceram. Int.* **2019**, *45*, 4283.
- [56] S. Saha, M. Jana, P. Khanra, P. Samanta, H. Koo, N. C. Murmu, T. Kuila, *ACS Appl. Mater. Interfaces* **2015**, *7*, 14211.
- [57] J. Guo, Y. Zhao, A. L. iu, T. Ma, *Electrochim. Acta* **2019**, *305*, 164.
- [58] G. A. M. Ali, O. A. Fouad, S. A. Makhlof, M. M. Yusoff, K. F. Chong, *J. Solid State Electrochem.* **2014**, *18*, 2505.
- [59] O. C. Pore, A. V. Fulari, R. K. Kamble, A. S. Shelake, N. B. Velhal, V. J. Fulari, G. M. Lohar, *J. Mater. Sci.: Mater. Electron.* **2021**, *32*, 20742.
- [60] J. Sun, Y. Wang, Y. Zhang, C. Xu, H. Chen, *Nanoscale Res. Lett.* **2019**, *14*, 340.
- [61] A. Noori, M. F. El-Kady, M. S. Rahmanifar, R. B. Kaner, M. F. Mousavi, *Chem. Soc. Rev.* **2019**, *48*, 1272.
- [62] M. Chandel, P. Makkar, N. N. Ghosh, *ACS Appl. Electron. Mater.* **2019**, *1*, 1215.
- [63] L. Sun, Q. Fu, C. Pan, *J. Hazard Mater.* **2021**, *410*, 124565.
- [64] S. L. Jadhav, A. L. Jadhav, P. B. Sarawade, B. K. Mandlikar, A. V. Kadam, *J. Energy Storage* **2024**, *82*, 110540.
- [65] J. Xu, T. Xiao, X. Tan, P. Xiang, L. Jiang, D. Wu, J. Li, S. Wang, *J. Alloys Compd.* **2017**, *706*, 351.
- [66] C. Zhang, L. Xie, W. Song, J. Wang, G. Sun, K. Li, *J. Electroanal. Chem.* **2013**, *706*, 1.
- [67] L. Liao, A. Zhang, K. Zheng, R. Liu, Y. Cheng, L. Wang, A. Li, J. Liu, *ACS Appl. Mater. Interfaces* **2021**, *13*, 28222.
- [68] Y. Li, P. Kamdem, X. J. Jin, *J. Alloys Compd.* **2021**, *850*, 156608.
- [69] M. Boota, M. Bécuwe, Y. Gogotsi, *ACS Appl. Energy Mater.* **2020**, *3*, 3144.
- [70] L. J. Xie, J. F. Wu, C. M. Chen, C. M. Zhang, L. Wan, J. L. Wang, Q. Q. Kong, C. X. Lv, K. X. Li, G. H. Sun, *J. Power Sources* **2013**, *242*, 148.
- [71] J. Li, X. Li, D. Xiong, L. Wang, D. Li, *Appl. Surf. Sci.* **2019**, *475*, 285.
- [72] C. Huang, C. Chen, M. Zhang, L. Lin, X. Ye, S. Lin, M. Antonietti, X. Wang, *Nat. Commun.* **2015**, *6*, 7698.
- [73] R. Samal, S. Mondal, A. S. Ganguly, B. Chakraborty, C. S. Rout, *Phys. Chem. Chem. Phys.* **2020**, *22*, 7903.
- [74] G. Kresse, J. Furthmüller, *Phys. Rev. B* **1996**, *54*, 11169.
- [75] G. Kresse, J. Furthmüller, *Comput. Mater. Sci.* **1996**, *6*, 15.
- [76] J. P. Perdew, K. Burke, M. Ernzerhof, *Phys. Rev. Lett.* **1996**, *77*, 3865.
- [77] S. Grimme, S. Ehrlich, L. Goerigk, *J. Comput. Chem.* **2011**, *32*, 1456.
- [78] Q. Zhou, W. Ju, Y. Yong, Q. Zhang, Y. Liu, J. Li, *Carbon* **2020**, *170*, 368.

Manuscript received: June 18, 2025

Revised manuscript received: July 14, 2025

Version of record online: